Acta Cryst A FOUNDATIONS ADVANCES
ISSN 2053-2733

Grazing-incidence small-angle X-ray scattering in a twofold rough-interface medium: a new theoretical approach using the q-eigenwave formalism

F. N. Chukhovskii* and B. S. Roshchin

Shubnikov Institute of Crystallography, Russian Academy of Sciences, Leninsky Prospect 59, Moscow, 119333, Russian Federation. *Correspondence e-mail: f_chukhov@yahoo.ca

Received 14 April 2015
Accepted 7 September 2015

Edited by W. F. Kuhs, Georg-August University Göttingen, Germany

Keywords: grazing-incidence small-angle X-ray scattering; statistically rough surface; eigenfunctions method.

Based on the rigorous Green function formalism to describe the grazing-incidence small-angle X-ray scattering (GISAXS) problem, a system of two linked integral equations is derived with respect to amplitudes of the reflected and transmitted plane **q**-eigenwaves (*eigenstate* functions) propagating through two homogeneous media separated from each other by a rough surface interface. To build up the coupled solutions of these basic equations beyond the perturbation theory constraint $2k\sigma\theta_0 < 1$, a simple iteration procedure is proposed as opposed to the self-consistent wave approach [Chukhovskii (2011). *Acta Cryst.* A**67**, 200–209; Chukhovski (2012). *Acta Cryst.* A**68**, 505–512]. Using the first-order iteration, analytical expressions for the averaged specular and non-specular scattering intensity distributions have been obtained. These expressions are further analysed in terms of the GISAXS parameters $\{k, \theta, \theta_0\}$ and surface finish ones $\{\sigma, \ell, h\}$, where θ and θ_0 are the scattering and incidence angles of the X-rays, respectively, σ is the root-mean-square roughness, ℓ is the correlation length, h is the fractal surface model index, $k = 2\pi/\lambda$, and λ is the X-ray wavelength. A direct way to determine the surface finish parameters from the experimental specular and diffuse scattering indicatrix scan data is discussed for an example of GISAXS measurements from rough surfaces of α-quartz and CdTe samples.

1. Introduction

Nowadays the grazing-incidence small-angle X-ray scattering (GISAXS) technique is widely used as a powerful tool for the systematic investigation into and study of solid and liquid surface interfaces, multilayered semiconductor nanostructures and optical mirrors. GISAXS is effective for control of finishing processes of optical surfaces in the length range with a precision of a few nanometres (see, *e.g.*, Church & Takacs, 1991; Asadchikov *et al.*, 2003; Pietsch *et al.*, 2004; Schmidbauer *et al.*, 2008; Renaud *et al.*, 2009).

Novel advanced technologies for fabricating X-ray optical devices require strict control of the surface perfection and, in turn, push ahead the GISAXS technique.

The latter allows one, at least, to get quantitative information such as the root-mean-square (r.m.s.) roughness σ and correlation length ℓ of rough surfaces in the scale from a few nanometres for the r.m.s. roughness σ up to some micrometres for correlation length ℓ (Pietsch *et al.*, 2004; Renaud *et al.*, 2009).

GISAXS studies are grounded in the theoretical works widely cited as Névot & Croce (1980), Petrashen' *et al.* (1983), Vinogradov *et al.* (1985), Sinha *et al.* (1988), de Boer (1994, 1995, 1996). In the work of Névot & Croce (1980) the statis-

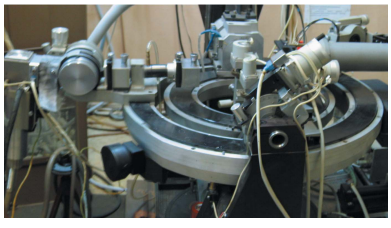

tical scattering factors that assign the reflected and transmitted specular intensities of the GISAXS waves propagating through the twofold rough-interface medium have been derived.

In order to investigate the GISAXS problem in the small-roughness approximation $2k\sigma\theta_0 < 1$, the rigorous Green function formalism (Andronov & Leontovich, 1926) has been applied in Vinogradov *et al.* (1985).

The theoretical GISAXS problem has been considered in detail in Sinha *et al.* (1988) where the distorted-wave Born approximation (DWBA) has been used to describe the specular and non-specular scattering waves propagating through the twofold rough-interface medium.

It should be mentioned that the theoretical GISAXS problem has been analysed in detail in Kozhevnikov & Pyatakhin (2000) and Kozhevnikov (2010), staying in the frame of the Green function formalism and the small-roughness approximation $2k\sigma\theta_0 < 1$ (hereafter, $k = 2\pi/\lambda$, λ is the X-ray wavelength, θ_0 is the incidence angle of the X-ray beam). Note that the above authors (Kozhevnikov & Pyatakhin, 2000, p. 256) have concluded that some additional assumptions (beyond the conventional DWBA approximation of quantum mechanics) have been used in the works of Sinha *et al.* (1988), de Boer (1994, 1995) and others. Such a conclusion, in turn, calls into question the plausibility of at least some results obtained therein.

Despite the generic attraction, there is a considerable obstacle in the implementation of the DWBA approach to the theoretical GISAXS problem, in particular a lack of the DWBA derivation, which follows *ab initio* from the Green function formalism (at least, we do not know any papers where it has been done).

Recently, with the use of high-order X-ray scattering in the frame of the Kirchhoff–Fresnel approach, attempts to go beyond the Debye–Waller approximation in calculations of the specular scattering factors have been made in Salikhov *et al.* (2011). In that method, the specular reflected and transmitted wave amplitudes are dependent both on the r.m.s. roughness σ and correlation length ℓ.

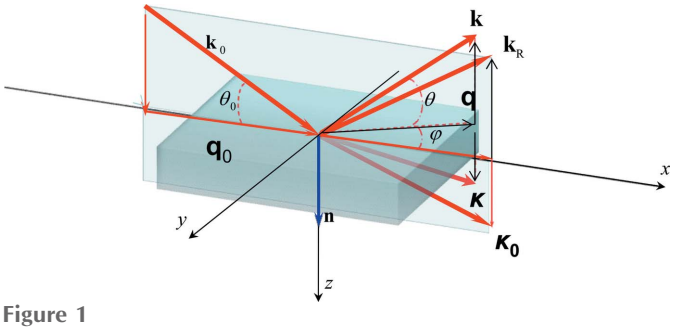

Figure 1
GISAXS layout: $\mathbf{k}_0 = \mathbf{q}_0 + k_z(q_0)\mathbf{n}$ is the incident wavevector; $\mathbf{k}_R = \mathbf{q}_0 - k_z(q_0)\mathbf{n}$ and $\boldsymbol{\kappa}_T = \mathbf{q}_0 + \kappa_z(q_0)\mathbf{n}$ are the wavevectors of the reflected and transmitted specular waves, respectively; $\mathbf{k}_R = \mathbf{q} - k_z(q)\mathbf{n}$ and $\boldsymbol{\kappa}_T = \mathbf{q} + \kappa_z(q)\mathbf{n}$ are the wavevectors of the reflected and transmitted non-specular waves, respectively. $\mathbf{n}$ is the unit vector along the z axis perpendicular to the reference plane $z = 0$; the lateral vectors $\mathbf{q}$ and $\mathbf{q}_0$ lie within the reference plane $z = 0$ ($\varphi = 0$ in the specular case).

Trying to go beyond the small-roughness approximation, $2k\sigma\theta_0 < 1$, the self-consistent wave approach (SCWA) based on the Green function formalism has been proposed in Chukhovskii (2011). In addition, to justify the SCWA, special attention is paid to bind the SCWA solutions in such a manner that they satisfy the optical theorem for the large-roughness parameter $2k\sigma\theta_0 \geq 1$ (Chukhovskii, 2012). Indeed, the fact that the GISAXS solutions should satisfy the optical theorem is the sole criterion of correctness for the theoretical approach. In this respect, it should be mentioned that the DWBA solutions (Sinha *et al.*, 1988; de Boer, 1995) fail to satisfy the optical theorem.

Clearly, it is desirable to achieve a modification of the GISAXS theory for the case of the large-roughness parameter $2k\sigma\theta_0 \geq 1$, where the perturbation theory approach is evidently not effective. In other words, the relevant GISAXS theory beyond the constraint $2k\sigma\theta_0 < 1$ is still of great interest.

In the present paper, we report on a novel modification of the GISAXS theory based on the Green function formalism. It is based on a series expansion of the GISAXS wavefield over the *eigenstate*-function waves, the so-called plane **q**-eigenwaves. The latter are nothing but the plane waves propagating on both sides of two homogeneous media separated from each other by a rough surface interface.

The present paper is organized as follows. In §2, following Chukhovskii (2011), the Green function formalism is briefly reproduced for completeness. The Green function is nothing but the two-dimensional Fourier integral of the product of the two linearly independent Fresnel solutions corresponding to the *direct* and *mirror-reversed* scattering geometry for the flat surface interface ($z = 0$) that separates the two homogeneous media.

In §3, the two linked integral equations to determine non-averaged amplitudes of the reflected and transmitted plane **q**-eigenwaves are obtained by the use of an expansion of the GISAXS wavefield over these **q**-eigenwaves propagating on both sides of the two homogeneous media. Then, staying in the scope of the first-order iteration procedure, a solution of these basic equations is built up. In this case, the zero-order iteration solutions are nothing but the conventional Fresnel amplitudes for the specular GISAXS waves propagating through the twofold planar-interface medium.

In §4, the statistically averaged solution for the reflected intensity distribution $dR_{tot}(\theta, \varphi; \theta_0)/d\Omega$ being the superposition of the specular and non-specular GISAXS wave components is derived (hereafter, θ is the scattering polar angle of the reflected beam and φ is the scattering azimuth angle of the reflected beam, see Fig. 1). To obtain it, we have utilized the Gaussian statistical model of a rough isotropic surface in terms of the r.m.s. roughness σ and the *cumulant* correlation function $K_2(|\mathbf{x}_1 - \mathbf{x}_2|)$ in the sense of the famous Kato paper (Kato, 1980). Analytical expressions are derived for the specular reflectivity $R_{spe}(\theta_0)$, non-specular intensity distribution $dR/d\Omega(\theta, \varphi; \theta_0)$ and diffuse scattering indicatrix (DSI) $dR/d\theta(\theta; \theta_0)$.

Hereafter, it is assumed that the grazing-incidence angle θ_0 is fixed and then, for simplicity, it has been omitted

in the following expressions of $dR/d\Omega(\theta, \varphi; \theta_0)$ and $dR/d\theta(\theta; \theta_0)$.

In §5, bearing in mind the description of the measured specular reflectivity $R_{spe}(\theta_0)$ and non-specular DSI $dR/d\theta(\theta)$ (see §6), the numerically simulated results for the distributions $R_{spe}(\theta_0)$, $dR/d\Omega(\theta, \varphi)$ and $dR/d\theta(\theta)$ are presented and analysed depending on the parameters $\{k\sigma, k\ell, \theta_0/\theta_{cr}\}$ of interest for various values of the fractal surface model index (FSMI) h = 1/4, 1/2, 3/4.

In §6, results of the specular and non-specular GISAXS measurements are presented for α-quartz and CdTe samples (the reference surface planes are $\{11\bar{2}0\}$ and $\{111\}$, respectively). The experimental data are analysed in terms of the present approach to directly determine the surface finish parameters such as the r.m.s. roughness σ, correlation length ℓ and FSMI h, not using any of the least-square iterative techniques in a χ^2 fashion (*cf. e.g.* Chukhovskii, 2009).

2. Theoretical background and notations. The Green function formalism

Here, for completeness of the theoretical description, we repeat the main milestones of a mathematics based on the Green function formalism (*cf.* Vinogradov *et al.*, 1985; Chukhovskii, 2011).

Accordingly, the scalar wave equation may be properly rewritten in the integral form

$$E(\mathbf{r}) = E_0(\mathbf{r}) - k^2 \int d^3\mathbf{r}' G(\mathbf{r}, \mathbf{r}') \Delta\chi(\mathbf{r}') E(\mathbf{r}'), \qquad (1)$$

where

$$\Delta\chi(\mathbf{r}') = \chi\{\Theta[z' - h(\mathbf{x}')] - \Theta(z')\}$$

with $h(\mathbf{x})$ being the surface height at the point $\mathbf{x}$.

Herein, the Green (point-source) function $G(\mathbf{r}, \mathbf{r}')$ is given by

$$G(\mathbf{r}, \mathbf{r}') = -i(4\pi)^{-2} \int d^2\mathbf{q}\left[k_z^{-1}(q) + \kappa_z^{-1}(q)\right] \times \exp[i\mathbf{q}(\mathbf{x} - \mathbf{x}')] \begin{cases} y_2(z, q) y_1(z', q), & z \le z' \\ y_1(z, q) y_2(z', q), & z \ge z' \end{cases} \qquad (2)$$

everywhere in the twofold medium with the step-like electric susceptibility $\chi(\mathbf{r}) = \chi\,\Theta(z)$; $\Theta(z)$ is the Heaviside function: $\Theta(z) = 1$ for $z > 0$ and $\Theta(z) = 0$ for $z < 0$.

Hereafter, χ is the complex electric susceptibility; $\chi = \mathrm{Re}\chi + i\mathrm{Im}\chi$, $\mathrm{Re}\chi < 0$ and $\mathrm{Im}\chi < 0$; $\theta_{cr} = (-\mathrm{Re}\chi)^{1/2}$ is the critical angle (typically, in the case of hard X-ray radiation with wavelength λ of the order of 0.1 nm $\mathrm{Re}\chi \cong -10^{-5}$, $\mathrm{Im}\chi \cong -0.05\mathrm{Re}\chi$).

Functions $y_1(z, q)$ and $y_2(z, q)$ are the two linearly independent solutions of the wave equation

$$d^2y/dz^2 + \{k^2[1 + \chi\Theta(z)] - q^2\}y = 0 \qquad (3)$$

relative to the variable z (the z axis is perpendicular to the reference plane $z = 0$).

They represent the conventional Fresnel solutions

$$y_1(z, q) = \begin{cases} \exp[ik_z(q)z] + R_1(q)\exp[-ik_z(q)z] & \text{for } z \le 0 \\ T_1(q)\exp[i\kappa_z(q)z] & \text{for } z \ge 0 \end{cases} \qquad (4a)$$

and

$$y_2(z, q) = \begin{cases} T_2(q)\exp[-ik_z(q)z] & \text{for } z \le 0 \\ \exp[-i\kappa_z(q)z] + R_2(q)\exp[i\kappa_z(q)z] & \text{for } z \ge 0 \end{cases} \qquad (4b)$$

in the *direct* and *mirror-reversed* GISAXS geometry, respectively.

The reflection, $R_1(q)$ and $R_2(q)$, and transmission, $T_1(q)$ and $T_2(q)$, coefficients take the form

$$R_1(q) = \frac{k_z(q) - \kappa_z(q)}{k_z(q) + \kappa_z(q)} \quad \text{and} \quad R_2(q) = \frac{\kappa_z(q) - k_z(q)}{k_z(q) + \kappa_z(q)},$$
$$T_1(q) = \frac{2k_z(q)}{k_z(q) + \kappa_z(q)} \quad \text{and} \quad T_2(q) = \frac{2\kappa_z(q)}{k_z(q) + \kappa_z(q)}, \qquad (5)$$

where the wavevector components $k_z(q)$ and $\kappa_z(q)$ equal to

$$k_z(q) = (k^2 - q^2)^{1/2}, \quad \kappa_z(q) = (\kappa^2 - q^2)^{1/2} \qquad (6)$$

relate to the same lateral vector $\mathbf{q}$ parallel to the reference plane $z = 0$; $\kappa^2 = k^2(1 + \chi)$.

The free term $E_0(\mathbf{r})$ on the right-hand side of the integral wave equation (1) takes the form

$$E_0(\mathbf{r}) = \exp(i\mathbf{q}_0\mathbf{x}) y_1(z, q_0) \qquad (7)$$

corresponding to the *incident* plane wave $E_{inc}(\mathbf{r}) = \exp(i\mathbf{k}_0\mathbf{r})$.

It should be mentioned that the integration range over the variable z' on the right-hand side of the integral wave equation (1) is given by the restricted interval, where the function of $\Theta[z' - h(\mathbf{x}')] - \Theta(z')$ differs from zero, which, in turn, determines the behaviour of the reflected and transmitted waves at infinity $z \to \mp\infty$.

3. Linked integral equations in terms of the plane q-eigenwaves for exploring the GISAXS phenomenon

Accordingly, the asymptotic GISAXS solutions for $z \to \mp\infty$ can be cast in the form

$$E_R(\mathbf{x}, z)\big|_{z\to-\infty} = R_1(q_0)\exp[i(\mathbf{q}_0\mathbf{x} - k_z z)] + \frac{i}{2\pi}\int \frac{d^2\mathbf{q}}{k_z(q)} \times \exp[i\mathbf{q}\mathbf{x} - ik_z(q)z] A_R(\mathbf{q}, \mathbf{q}_0), \qquad (8a)$$

$$E_T(\mathbf{x}, z)\big|_{z\to\infty} = T_1(q_0)\exp[i(\mathbf{q}_0\mathbf{x} + \kappa_z z)] + \frac{i}{2\pi}\int \frac{d^2\mathbf{q}}{\kappa_z(q)} \times \exp[i\mathbf{q}\mathbf{x} + i\kappa_z(q)z] A_T(\mathbf{q}, \mathbf{q}_0), \qquad (8b)$$

where the scattering amplitudes $A_R(\mathbf{q}, \mathbf{q}_0)$ and $A_T(\mathbf{q}, \mathbf{q}_0)$ are introduced as

$$A_R(\mathbf{q}, \mathbf{q}_0) = -\frac{\chi k^2}{4\pi}\int d^2\mathbf{x}\exp(-i\mathbf{q}\mathbf{x}) \int_0^{h(\mathbf{x})} dz y_1(z, q) E(\mathbf{x}, z), \qquad (9a)$$

$$A_{\rm T}(\mathbf{q},\mathbf{q}_0) = -\frac{\chi k^2}{4\pi}\int \mathrm{d}^2\mathbf{x}\exp(-i\mathbf{q}\mathbf{x})\int\limits_0^{h(\mathbf{x})}\mathrm{d}z\, y_2(z,q)E(\mathbf{x},z). \tag{9b}$$

Further, one uses the Fourier representation of the GISAXS wavefield $E(\mathbf{x},z)$ in the form of the series expansion in reciprocal space over the plane $\mathbf{q}$-eigenwaves, namely:

$$E(\mathbf{x},z) = \frac{1}{(2\pi)^2}\int \mathrm{d}^2\mathbf{q} \times \left\{\begin{array}{ll} (2\pi)^2\delta_2(\mathbf{q}-\mathbf{q}_0)\exp[i\mathbf{q}\mathbf{x}+ik_z(q)z] + B(\mathbf{q})\exp[i\mathbf{q}\mathbf{x}-ik_z(q)z] & \text{for } z<h(\mathbf{x}) \\ C(\mathbf{q})\exp[i\mathbf{q}\mathbf{x}+i\kappa_z(q)z] & \text{for } z>h(\mathbf{x}) \end{array}\right\}. \tag{10}$$

By combining equations (8*a*), (8*b*)–(10) to determine the plane $\mathbf{q}$-eigenwave amplitudes $B(\mathbf{q})$ and $C(\mathbf{q})$, one can readily find the following system of two integral equations:

$$B(\mathbf{q}) = (2\pi)^2\delta_2(\mathbf{q}-\mathbf{q}_0)R_1(q_0) - \frac{i\chi k^2}{2(2\pi)^2 k_z(q)} \times \int \mathrm{d}^2\mathbf{x}\exp(-i\mathbf{q}\mathbf{x})\int \mathrm{d}^2\mathbf{q}_1\int\limits_0^{h(\mathbf{x})}\mathrm{d}z\, y_1(z,q) \times \left\{\begin{array}{ll} \left.\begin{array}{l}(2\pi)^2\delta_2(\mathbf{q}_1-\mathbf{q}_0)\exp[i\mathbf{q}_1\mathbf{x}+ik_z(q_1)z]+ \\ B(\mathbf{q}_1)\exp[i\mathbf{q}_1\mathbf{x}-ik_z(q_1)z]\end{array}\right) & \text{for } h(\mathbf{x})>0, \\ C(\mathbf{q}_1)\exp[i\mathbf{q}_1\mathbf{x}+i\kappa_z(q_1)z] & \text{for } h(\mathbf{x})<0 \end{array}\right\}, \tag{11a}$$

$$C(\mathbf{q}) = (2\pi)^2\delta_2(\mathbf{q}-\mathbf{q}_0)T_1(q_0) - \frac{i\chi k^2}{2(2\pi)^2 \kappa_z(q)} \times \int \mathrm{d}^2\mathbf{x}\exp(-i\mathbf{q}\mathbf{x})\int \mathrm{d}^2\mathbf{q}_1\int\limits_0^{h(\mathbf{x})}\mathrm{d}z\, y_2(z,q) \times \left\{\begin{array}{ll} \left.\begin{array}{l}(2\pi)^2\delta_2(\mathbf{q}_1-\mathbf{q}_0)\exp[i\mathbf{q}_1\mathbf{x}+ik_z(q_1)z]+ \\ B(\mathbf{q}_1)\exp[i\mathbf{q}_1\mathbf{x}-ik_z(q_1)z]\end{array}\right) & \text{for } h(\mathbf{x})>0, \\ C(\mathbf{q}_1)\exp[i\mathbf{q}_1\mathbf{x}+i\kappa_z(q_1)z] & \text{for } h(\mathbf{x})<0 \end{array}\right\}. \tag{11b}$$

Further, inserting expressions (4*a*), (4*b*)–(6) into equations (11*a*), (11*b*), the straightforward routine calculations yield a system of two integral equations:

$$\begin{aligned} B(\mathbf{q}) = {} & (2\pi)^2\delta_2(\mathbf{q}-\mathbf{q}_0)R_1(q_0) - \frac{\chi k^2}{(2\pi)^2 2k_z(q)}\int \mathrm{d}^2\mathbf{q}_1\int \mathrm{d}^2\mathbf{x}\exp(-i(\mathbf{q}-\mathbf{q}_1)\mathbf{x}) \\ & \times\left[T_1(q)\left((2\pi)^2\delta_2(\mathbf{q}_1-\mathbf{q}_0)\left[\frac{\exp(i(\kappa_z(q)+k_z(q_1))h(\mathbf{x}))-1}{(\kappa_z(q)+k_z(q_1))}\right]\right.\right. \\ & \left.+B(\mathbf{q}_1)\left[\frac{\exp(i(\kappa_z(q)-k_z(q_1))h(\mathbf{x}))-1}{(\kappa_z(q)-k_z(q_1))}\right]\right)\Theta[h(\mathbf{x})] \\ & + C(\mathbf{q}_1)\left(\frac{\exp(i(k_z(q)+\kappa_z(q_1))h(\mathbf{x}))-1}{(k_z(q)+\kappa_z(q_1))}\right. \\ & \left.\left.+R_1(q)\frac{\exp(i(\kappa_z(q_1)-k_z(q))h(\mathbf{x}))-1}{(\kappa_z(q_1)-k_z(q))}\right)\Theta[-h(\mathbf{x})]\right] \end{aligned} \tag{12a}$$

$$\begin{aligned} C(\mathbf{q}) = {} & (2\pi)^2\delta_2(\mathbf{q}-\mathbf{q}_0)T_1(q_0) - \frac{\chi k^2}{(2\pi)^2 2\kappa_z(q)}\int \mathrm{d}^2\mathbf{q}_1\int \mathrm{d}^2\mathbf{x}\exp(-i(\mathbf{q}-\mathbf{q}_1)\mathbf{x}) \\ & \times\left[\left((2\pi)^2\delta_2(\mathbf{q}_1-\mathbf{q}_0)\left(\frac{\exp(-i(\kappa_z(q)-k_z(q_1))h(\mathbf{x}))-1}{-(\kappa_z(q)-k_z(q_1))}\right.\right.\right. \\ & \left.+R_2(q)\frac{\exp(i(\kappa_z(q)+k_z(q_1))h(\mathbf{x}))-1}{(\kappa_z(q)+k_z(q_1))}\right) \\ & + B(\mathbf{q}_1)\left(\frac{\exp(-i(\kappa_z(q)+k_z(q_1))h(\mathbf{x}))-1}{-(\kappa_z(q)+k_z(q_1))}\right. \\ & \left.\left.+R_2(q)\frac{\exp(i(\kappa_z(q)-k_z(q_1))h(\mathbf{x}))-1}{(\kappa_z(q)-k_z(q_1))}\right)\Theta[h(\mathbf{x})]\right. \\ & \left.+C(\mathbf{q}_1)T_2(q)\left(\frac{\exp(i(\kappa_z(q_1)-k_z(q))h(\mathbf{x}))-1}{(\kappa_z(q_1)-k_z(q))}\right)\Theta[-h(\mathbf{x})]\right] \end{aligned} \tag{12b}$$

relative to the amplitudes $B(\mathbf{q})$ and $C(\mathbf{q})$ [$\delta_2(\mathbf{q}-\mathbf{q}_0)$ is the two-dimensional delta function].

How can we get solutions of the two equations (12*a*), (12*b*) beyond the small-roughness approximation $2k\sigma\theta_0 < 1$? One is supposed to apply the general iteration procedure for building up the $\mathbf{q}$-eigenwave amplitudes $B(\mathbf{q})$ and $C(\mathbf{q})$. To do this, at each order of the n-step iteration we have to take into account the nth-order scattering of the $\mathbf{q}$-eigenwaves in the twofold rough medium.

Then, we put

$$\begin{aligned} B(\mathbf{q}) &= B_0(\mathbf{q}) + B_1(\mathbf{q}) + \ldots \text{ and } B_0(\mathbf{q}) = (2\pi)^2\delta_2(\mathbf{q}-\mathbf{q}_0)R_1(\mathbf{q}_0), \\ C(\mathbf{q}) &= C_0(\mathbf{q}) + C_1(\mathbf{q}) + \ldots \text{ and } C_0(\mathbf{q}) = (2\pi)^2\delta_2(\mathbf{q}-\mathbf{q}_0)T_1(\mathbf{q}_0). \end{aligned} \tag{13}$$

Inserting expansions (13) into equations (12*a*) and (12*b*) and confining ourselves by terms of the first-order iteration, one obtains the amplitudes $B_1(\mathbf{q})$ and $C_1(\mathbf{q})$:

$$\begin{aligned} B_1(\mathbf{q}) = {} & -\frac{\chi k^2}{2k_z(q)}\int \mathrm{d}^2\mathbf{x}\exp(-i(\mathbf{q}-\mathbf{q}_0)\mathbf{x}) \\ & \times\left[T_1(q)\left(\left[\frac{\exp(i(\kappa_z(q)+k_z(q_0))h(\mathbf{x}))-1}{(\kappa_z(q)+k_z(q_0))}\right]\right.\right. \\ & \left.+R_1(q_0)\left[\frac{\exp(i(\kappa_z(q)-k_z(q_0))h(\mathbf{x}))-1}{(\kappa_z(q)-k_z(q_0))}\right]\right)\Theta[h(\mathbf{x})] \\ & + T_1(q_0)\left(\frac{\exp(i(k_z(q)+\kappa_z(q_0))h(\mathbf{x}))-1}{(k_z(q)+\kappa_z(q_0))}\right. \\ & \left.\left.+R_1(q)\frac{\exp(i(\kappa_z(q_0)-k_z(q))h(\mathbf{x}))-1}{(\kappa_z(q_0)-k_z(q))}\right)\Theta[-h(\mathbf{x})]\right], \end{aligned} \tag{14a}$$

$$C_1(\mathbf{q}) = -\frac{\chi k^2}{2\kappa_z(q)}\int \mathrm{d}^2\mathbf{x}\exp(-i(\mathbf{q}-\mathbf{q}_0)\mathbf{x})$$
$$\times\Bigg[\Bigg(\Bigg(\frac{\exp(-i(\kappa_z(q)-k_z(q_0))h(\mathbf{x}))-1}{-(\kappa_z(q)-k_z(q_0))}$$
$$+R_2(q)\frac{\exp(i(\kappa_z(q)+k_z(q_0))h(\mathbf{x}))-1}{(\kappa_z(q)+k_z(q_0))}\Bigg)$$
$$+R_1(q_0)\Bigg(\frac{\exp(-i(\kappa_z(q)+k_z(q_0))h(\mathbf{x}))-1}{-(\kappa_z(q)+k_z(q_0))}$$
$$+R_2(q)\frac{\exp(i(\kappa_z(q)-k_z(q_0))h(\mathbf{x}))-1}{(\kappa_z(q)-k_z(q_0))}\Bigg)\Bigg)\Theta[h(\mathbf{x})]$$
$$+T_1(q_0)T_2(q)\Bigg(\frac{\exp(i(\kappa_z(q_0)-k_z(q))h(\mathbf{x}))-1}{(\kappa_z(q_0)-k_z(q))}\Bigg)\Theta[-h(\mathbf{x})]\Bigg]. \quad (14b)$$

It should be mentioned that the complex terms on the right-hand sides of expressions (14*a*) and (14*b*) are the partial scattering amplitudes for the plane **q**-eigenwaves, propagating through the twofold rough medium (*cf.* Chukhovskii, 2011).

Hereafter, for simplicity we will consider only the reflected **q**-eigenwaves. Following Chukhovskii (2011), an expression for the entire reflected intensity distribution can be written as

$$\frac{\mathrm{d}R_{\mathrm{tot}}(\theta,\varphi)}{\mathrm{d}\Omega} = (2\pi)^{-2}k^2S_2^{-1}\frac{\sin^2\theta}{\sin\theta_0}\overline{|B(\mathbf{q})|^2}, \quad (15)$$

where the symbol $\overline{|\ldots|^2}$ denotes the ensemble average procedure, $\mathrm{d}\Omega = \cos\theta\mathrm{d}\theta\mathrm{d}\varphi$ is the elementary solid angle for the reflected beam, S_2 is an area of a rough surface impinged on by the incident X-ray beam.

As it follows from equation (15), the intensity distribution $\mathrm{d}R_{\mathrm{tot}}(\theta,\varphi)/\mathrm{d}\Omega$ is divided into the two terms

$$\frac{\mathrm{d}R_{\mathrm{tot}}(\theta,\varphi)}{\mathrm{d}\Omega} = \frac{\mathrm{d}R_{\mathrm{spec}}(\theta,\varphi)}{\mathrm{d}\Omega} + \frac{\mathrm{d}R(\theta,\varphi)}{\mathrm{d}\Omega}, \quad (16)$$

where the first term determines the specular intensity distribution

$$\frac{\mathrm{d}R_{\mathrm{spec}}(\theta,\varphi)}{\mathrm{d}\Omega} = (2\pi)^{-2}k^2S_2^{-1}\frac{\sin^2\theta}{\sin\theta_0}\left|B_0(\mathbf{q}) + \overline{B_1(\mathbf{q})}\right|^2 \quad (17a)$$

and the second one yields the non-specular intensity distribution

$$\frac{\mathrm{d}R(\theta,\varphi)}{\mathrm{d}\Omega} = (2\pi)^{-2}k^2S_2^{-1}\frac{\sin^2\theta}{\sin\theta_0}\overline{[B_1(\mathbf{q})B_1^*(\mathbf{q})]}|_{\mathrm{cum}}, \quad (17b)$$

on the right-hand side of equation (16).

Note that the expression (17*b*) for the non-specular intensity distribution is determined by the so-called *cumulant* average of bilinear combination $B_1(\mathbf{q})\cdot B_1^*(\mathbf{q})$ (Kato, 1980).

Using the Gaussian roughness statistics and introducing into consideration the $\mathrm{PSD}_{2\mathrm{D}}(|\mathbf{q}-\mathbf{q}_0|)$ function, the straightforward routine calculations yield the following robust expressions for the reflected specular and non-specular intensity distribution, respectively:

$$\frac{\mathrm{d}R_{\mathrm{spec}}(\theta,\varphi)}{\mathrm{d}\Omega} = k^2\sin\theta_0\delta_2(\mathbf{q}-\mathbf{q}_0)\left|R_1(q_0)\right|^2 f(q_0) \quad (18)$$

and

$$\frac{\mathrm{d}R(\theta,\varphi)}{\mathrm{d}\Omega} = \frac{|\chi|^2k^2\eta_R(q,q_0)}{16\pi^2\sin\theta_0}\mathrm{PSD}_{2\mathrm{D}}(|\mathbf{q}-\mathbf{q}_0|). \quad (19)$$

Then, as it follows from equations (18), (19) the specular reflectivity $R_{\mathrm{spec}}(\theta_0)$ is equal to

$$R_{\mathrm{spec}}(\theta_0) = |R_1(q_0)|^2 f(q_0) \quad (20)$$

and the corresponding expression for the DSI $\mathrm{d}R/\mathrm{d}\theta(\theta)$ takes the form $[\mathrm{d}R/\mathrm{d}\theta(\theta) = \cos\theta\int \mathrm{d}\varphi\,\mathrm{d}R/\mathrm{d}\Omega(\theta,\varphi)]$

$$\frac{\mathrm{d}R}{\mathrm{d}\theta}(\theta) = \frac{|\chi|^2\cos\theta\eta_R(q,q_0)}{16\pi^2\sin\theta_0}k^2\mathrm{PSD}_{1\mathrm{D}}(q,q_0). \quad (21)$$

Expressions for the $\mathrm{PSD}_{2\mathrm{D}}(|\mathbf{q}-\mathbf{q}_0|)$ and $\mathrm{PSD}_{1\mathrm{D}}(q,q_0)$ functions are given in Appendix *A*. Appropriately, expressions for the specular and non-specular scattering factors, namely $f(q_0)$ and $\eta_R(q,q_0)$, are given in Appendix *B*.

Before proceeding further, it is important to clarify some points of the present GISAXS theory approach beyond the constraint $2k\sigma\theta_0 < 1$.

First, the above analytical formulas (19)–(21) are derived in the scope of the first-order iteration procedure to solve the integral equations (12*a*), (12*b*). Note that the specular scattering factor $f(q_0)$ obtained in the form of equation (31) (*cf.* Appendix *B* for details) is different from the Debye–Waller factor $f_{\mathrm{DW}}(q_0)$. For this, both of them contain only the r.m.s. roughness σ-dependence.

It remains to be seen how well it will work if one takes into account the high-order scattering effects in a proper way. One thing is clear, that consideration of the high-order iterations must lead to the additional ℓ-dependence of the specular scattering factor $f(q_0)$. It is a good topic for future work to improve the present approach of the GISAXS theory. In this respect, it should be mentioned that the high-order scattering effects have been considered in Salikhov *et al.* (2011), where the specular scattering factor $f(q_0)$ becomes dependent on both the r.m.s. roughness σ and correlation length ℓ.

Second, when the ensemble averaging procedure is applied to obtain expressions (18) and (19) we assume the Gaussian statistics of roughness and the *K*-correlation model for a rough surface. In particular, we utilize the $\mathrm{PSD}_{2\mathrm{D}}(|\mathbf{q}-\mathbf{q}_0|)$ function in the form of equation (26), widely used in the GISAXS theory (Sinha *et al.*, 1988; de Boer, 1995, 1996; Church & Takacs, 1991; Asadchikov *et al.*, 2003; Renaud *et al.*, 2009).

It is clear that real rough surfaces, in general, do not satisfy the Gaussian roughness statistics and the *K*-correlation model, and one needs to utilize more realistic many-level models. At present, we can state that the current theoretical approach does work and can be applied, provided that the proper statistical model adequately describing a peculiar rough surface is chosen.

Analytical formulas (20), (21) represent the theoretical basis to interpret the specular $R_{\mathrm{spec}}(\theta_0)$ and non-specular $\mathrm{d}R/\mathrm{d}\theta(\theta)$ scan data obtained in GISAXS experiments.

Concerning the formula (20) for the specular reflectivity $R_{spec}(\theta_0)$, and how it follows from expression (31), the specular scattering factor $f(q_0)$ apparently is equal to the Debye–Waller factor $f_{DW}(q_0) = \exp[-4k_z^2(q_0)\sigma^2]$, provided that $|k_z(q_0) - \kappa_z(q_0)|^2\sigma^2 \ll \exp[-2k_z^2(q_0)\sigma^2]$.

In the opposite case, when the inequality $\exp[-2k_z^2(q_0)\sigma^2] \ll |k_z(q_0) - \kappa_z(q_0)|^2\sigma^2 \ll 1$ takes place, the specular scattering factor $f(q_0)$ is about equal to $0.25|k_z(q_0) - \kappa_z(q_0)|^4\sigma^4 \ll 1$ with accuracy up to $\exp[-2k_z^2(q_0)\sigma^2] \ll 1$.

On the other hand, staying within the total reflection region, $\theta_0 < \theta_{cr}$, along with the small r.m.s. roughness σ, when both the inequalities $|k_z(q_0) \pm \kappa_z(q_0)|\sigma < 1$ take place, the specular scattering factor $f(q_0)$ is equal to the Névot–Croce factor of $1 - 4k_z(q_0)\mathrm{Re}\lfloor\kappa_z(q_0)\rfloor\sigma^2$ unlike the Debye–Waller factor of $1 - 4k_z^2(q_0)\sigma^2$.

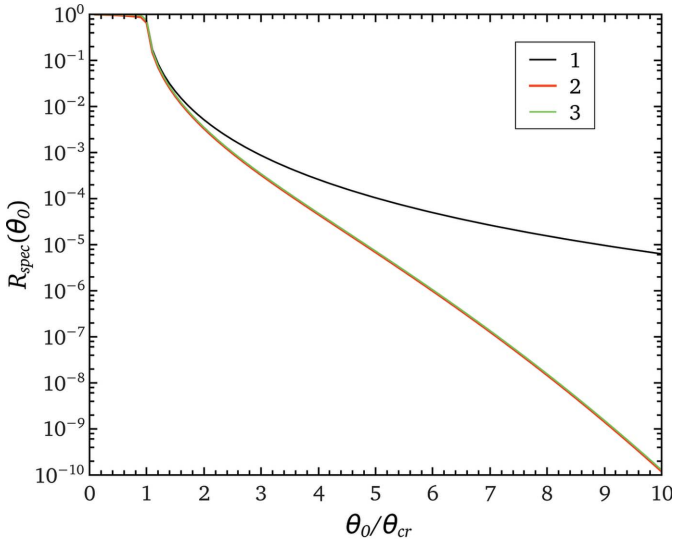

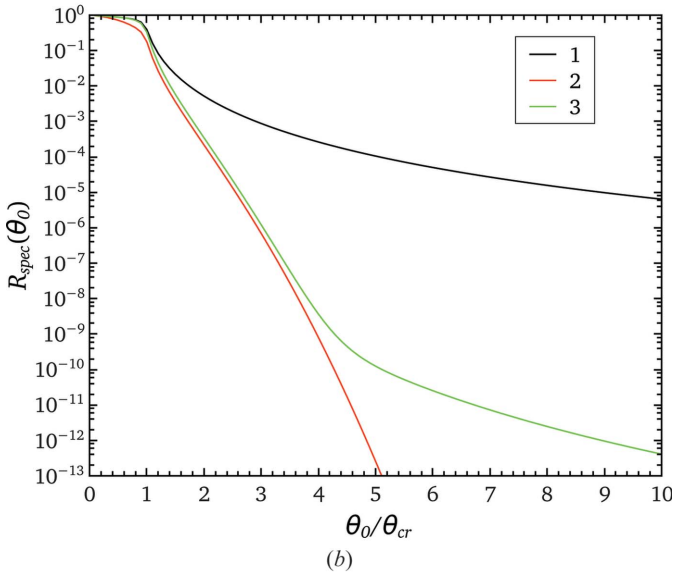

Figure 2
Specular scans $R_{spe}(\theta_0)$ numerically simulated *versus* grazing-incidence angle θ_0: 1, Fresnel; 2, Debye–Waller; 3, present approach. (*a*) α-Quartz sample, reference surface $\{11\bar{2}0\}$; (*b*) CdTe sample, reference surface {111}. The r.m.s. roughness $k\sigma$: (*a*) = 40; (*b*) = 80. Incident X-ray Cu $K\alpha_1$ radiation.

Further, we will discuss some features of expressions (19) and (21) for the non-specular intensity distribution $dR/d\Omega(\theta, \varphi)$ and DSI $dR/d\theta(\theta)$, respectively.

First, it is seen from formulas (19) and (21), they both contain the same statistical non-specular scattering factor $\eta_R(q, q_0)$ that is given by expression (32) along with (33)–(35) (*cf.* Appendix *B* for details) . As it follows from equations (32)–(35), the factor $\eta_R(q, q_0)$ only depends on the r.m.s. roughness σ. From the physical viewpoint, such a feature has to remain in general for any roughness statistics and correlation model of a rough surface. In our case the ℓ-dependence of the DSI [equation (21)] arising due to the $PSD_{1D}(q, q_0)$ is determined by the *K*-correlation model we use [*cf.* equation (30)].

In-depth analysis of expressions (33)–(35) shows that in the case of the small-roughness approximation $2k\sigma\theta_0 < 1$ the statistical scattering factor $\eta_R(q, q_0)$ reduces to the corresponding one in Vinogradov *et al.* (1985), provided that the inequality $\max[|\alpha|, |\beta|, |\mu|, |\nu|] \ll 1$ holds (*cf.* Chukhovskii, 2011). Thus, the statistical scattering factor $\eta_R(q, q_0)$ has a maximum whenever the angles θ or θ_0 are equal to θ_{cr}. It is interesting that the presence of a maximum on $\eta_R(q, q_0)$ at the scattering angle θ close to θ_{cr} remains even if the aforementioned inequality fails (see the numerical calculations in the next section). As a result, the non-specular intensity distributions [equations (19) and (21)] have a 'Yoneda scattering' peak at angle $\theta = \theta_{cr}$ (Yoneda, 1963). It is clear that the 'Yoneda scattering' peak height depends on the angular width of the corresponding $PSD_{2D}(q, q_0)$, $PSD_{1D}(q, q_0)$ functions, which in turn are given by the correlation length parameter $k\ell$ [see equations (26) and (30), *cf.* Appendix *A*].

Loosely speaking, while one stays in the frame of the *K*-correlation model, together both formulas (20) and (21) may be applied to restore all the surface finish parameters such as $\{k\sigma, k\ell, h\}$ from the measured scan data, for instance, with the use of one of the least-square iterative algorithms [see, *e.g.*, dynamic parameter-retrieval algorithm (Chukhovskii, 2009)].

However, we can point out a simple way to adjust theoretical expressions (20) and (21) to corresponding experimental scans and, in particular, to extract the FSMI *h* by not applying the least-square iterative algorithm.

So, we can use the asymptotic straight-line behaviour of the theoretical expression (21) in the log–log scale for large scattering angles θ, $\theta \gg \theta_0 > \theta_{cr}$ (*cf.* Church & Takacs, 1991; Wong *et al.*, 1991).

It is rather simple to show that, with an increase of scattering angle θ, when $\theta \gg \theta_0$, the parameters involved in equation (35) tend asymptotically to the values

$$\mathrm{Re}(\alpha) \simeq \mathrm{Re}(\beta) \simeq \mathrm{Re}(\mu) \simeq -\mathrm{Re}(\nu) \cong 2^{-1/2}k_z(q)\sigma \gg 1,$$
$$\mathrm{Im}(\alpha) \simeq \mathrm{Im}(\beta) \simeq \mathrm{Im}(\mu) \simeq -\mathrm{Im}(\nu) \ll 1$$

and, therefore, the factor $\eta_R(q, q_0)$ decreases as

$$\eta_R(q, q_0)|_{\theta/\theta_0 \gg 1} \propto (\theta/\theta_0)^{-2}. \qquad (22)$$

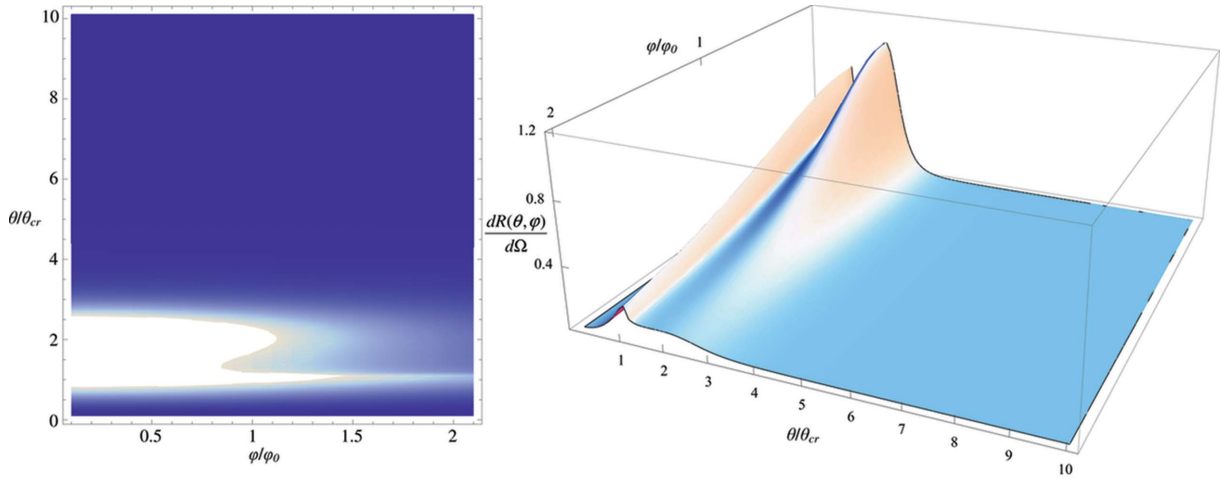

(*a*)

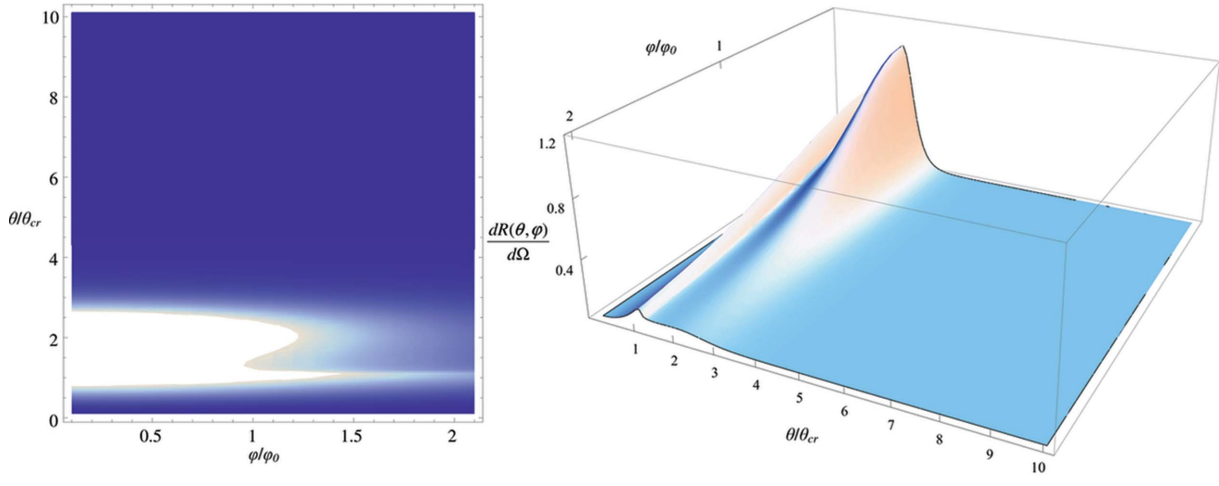

(*b*)

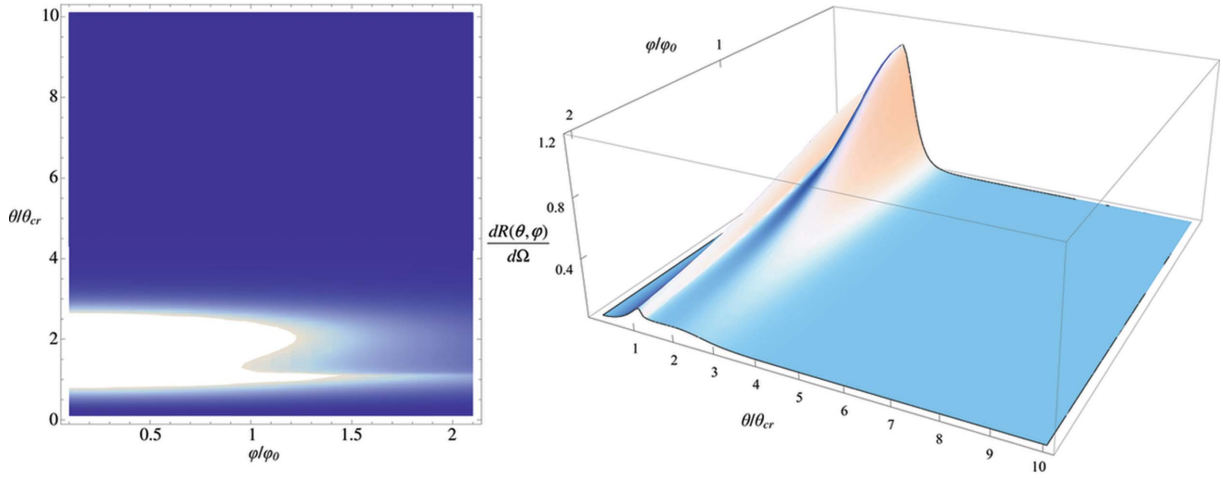

(*c*)

Figure 3
Normalized scans $[dR/d\Omega(\theta, \varphi)]/[dR/d\Omega(\theta_0, \varphi = 0)]$. Grazing-incidence angle θ_0/θ_{cr} is equal to 2. The r.m.s. roughness $k\sigma$ is equal to 40. Scattering polar and azimuth angles (θ, φ) are measured in units of (θ_{cr}, φ_0), $\theta_{cr} = (-\mathrm{Re}\,\chi)^{1/2} = 10^{-2.5}$ and $\varphi_0 = (k\ell)^{-1} = (5)^{-1}10^{-4}$; fractal index h is equal to 1/4 (*a*), 1/2 (*b*), 3/4 (*c*).

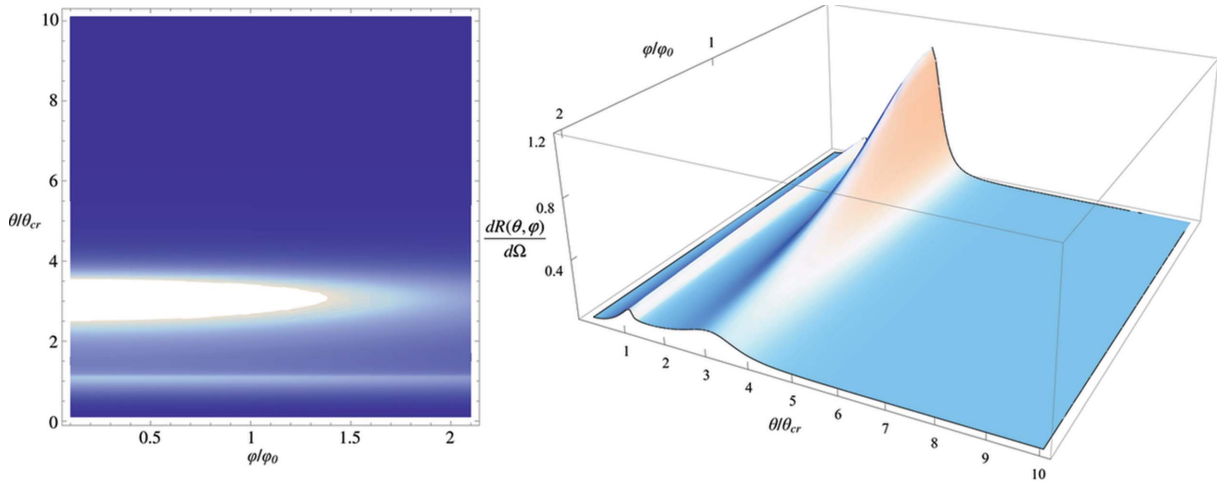

(*a*)

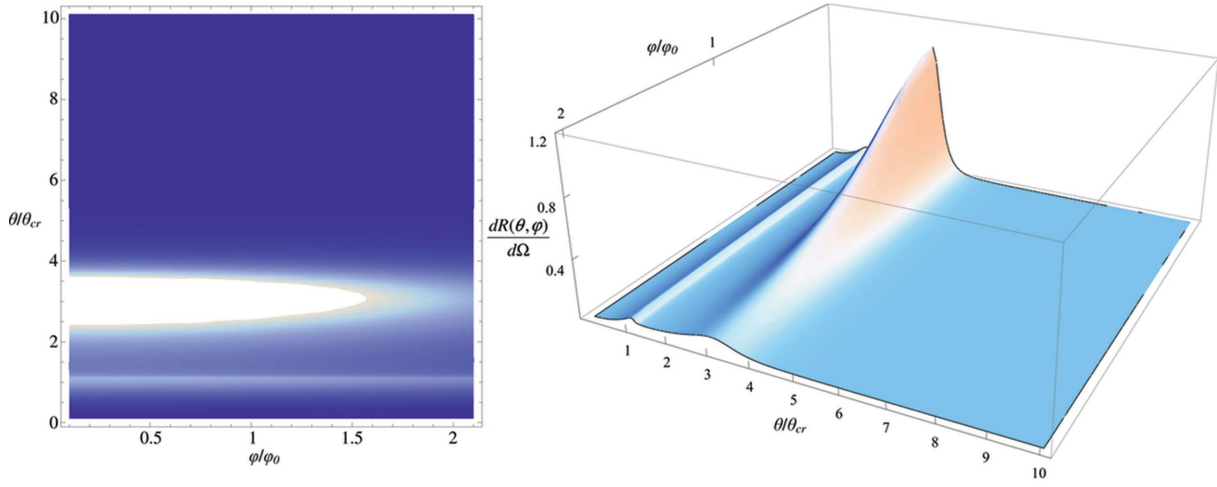

(*b*)

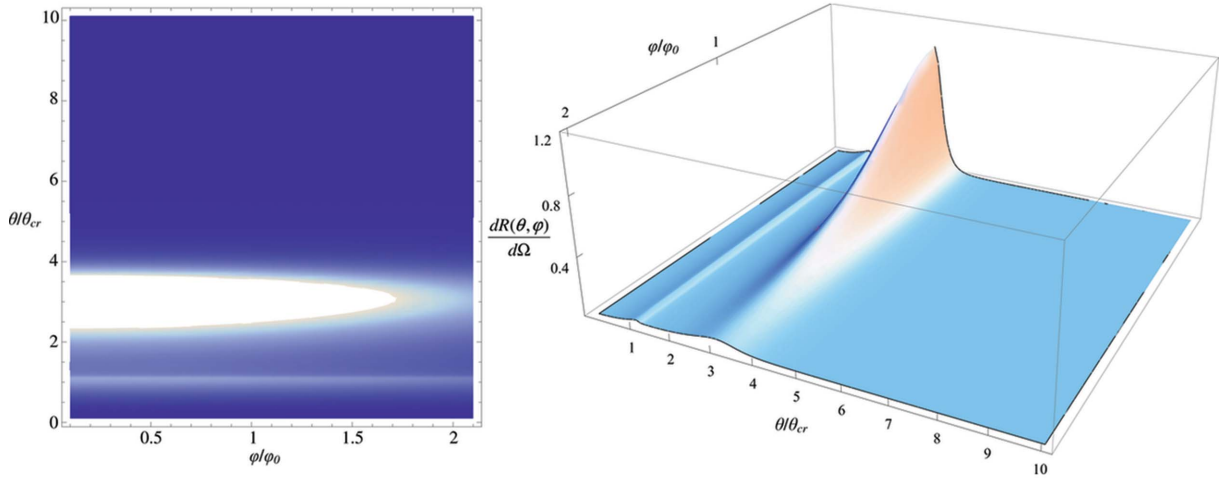

(*c*)

Figure 4
Normalized scans $[dR/d\Omega(\theta, \varphi)]/[dR/d\Omega(\theta_0, \varphi = 0)]$. Grazing-incidence angle θ_0/θ_{cr} is equal to 3. The r.m.s. roughness $k\sigma$ is equal to 40. Scattering polar and azimuth angles (θ, φ) are measured in units of (θ_{cr}, φ_0), $\theta_{cr} = (-\mathrm{Re}\chi)^{1/2} = 10^{-2.5}$ and $\varphi_0 = (k\ell)^{-1} = (5)^{-1}10^{-4}$; fractal index h is equal to 1/4 (*a*), 1/2 (*b*), 3/4 (*c*).

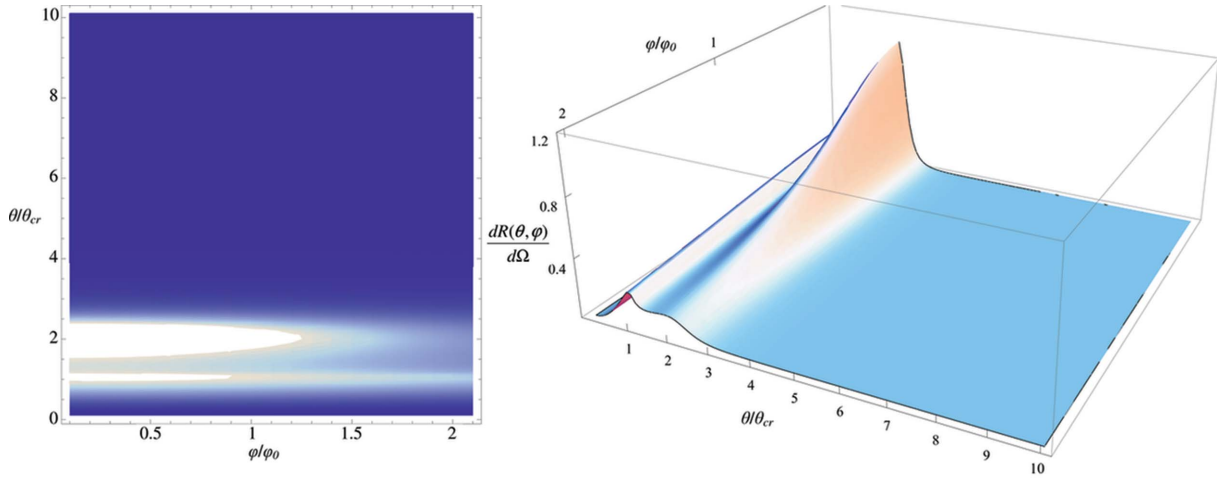

(*a*)

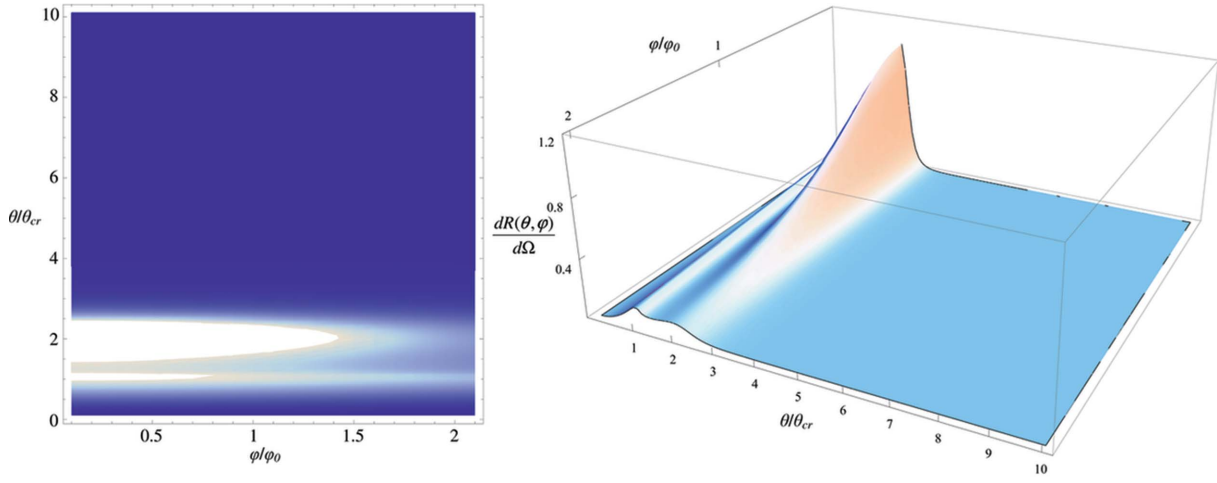

(*b*)

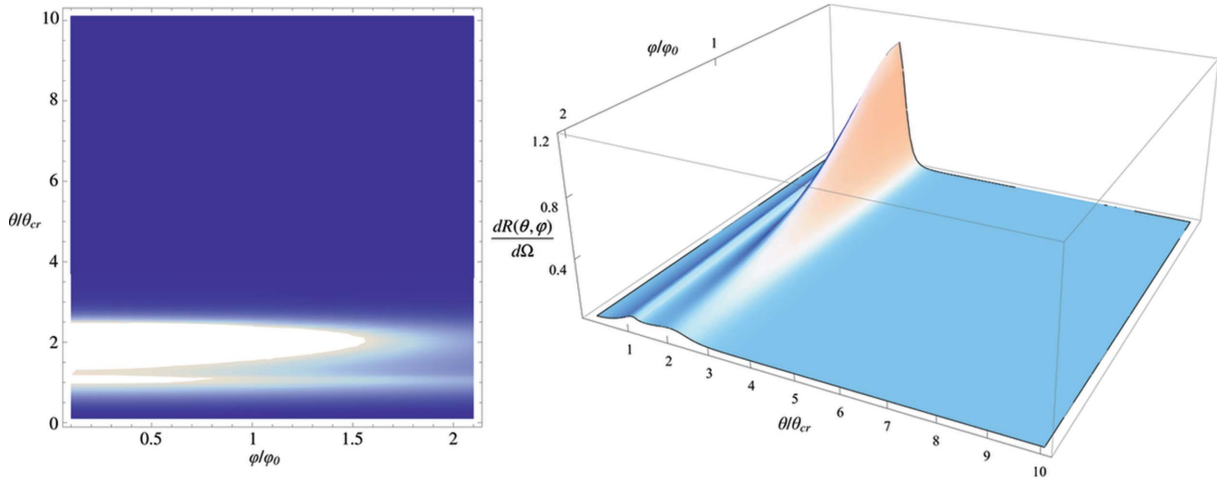

(*c*)

Figure 5
Normalized scans $[dR/d\Omega(\theta, \varphi)]/[dR/d\Omega(\theta_0, \varphi = 0)]$. Grazing-incidence angle θ_0/θ_{cr} is equal to 2. The r.m.s. roughness $k\sigma$ is equal to 80. Scattering polar and azimuth angles (θ, φ) are measured in units of (θ_{cr}, φ_0), $\theta_{cr} = (-\mathrm{Re}\chi)^{1/2} = 10^{-2.5}$ and $\varphi_0 = (k\ell)^{-1} = (5)^{-1}10^{-4}$; fractal index h is equal to 1/4 (*a*), 1/2 (*b*), 3/4 (*c*).

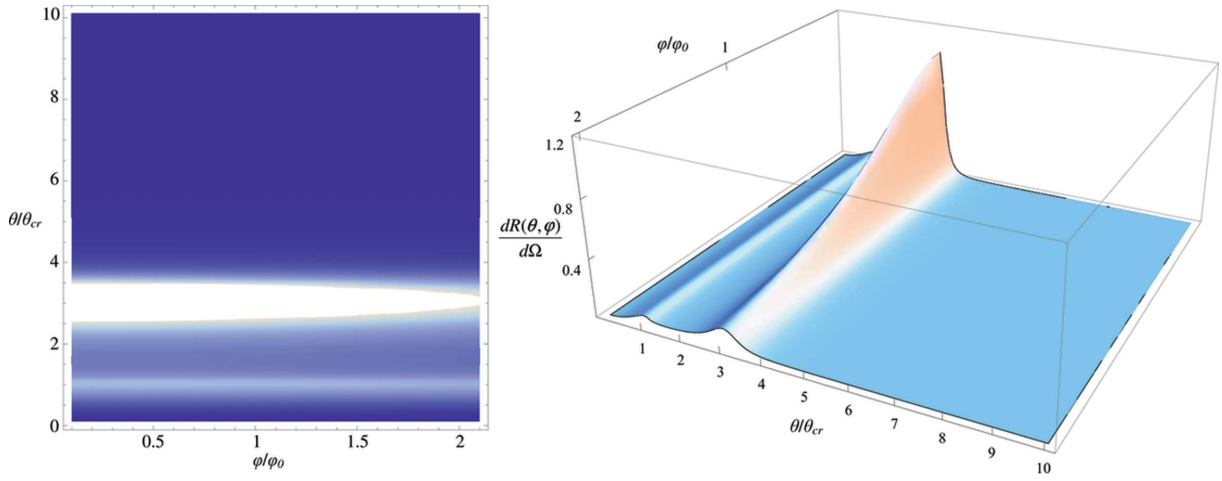

(*a*)

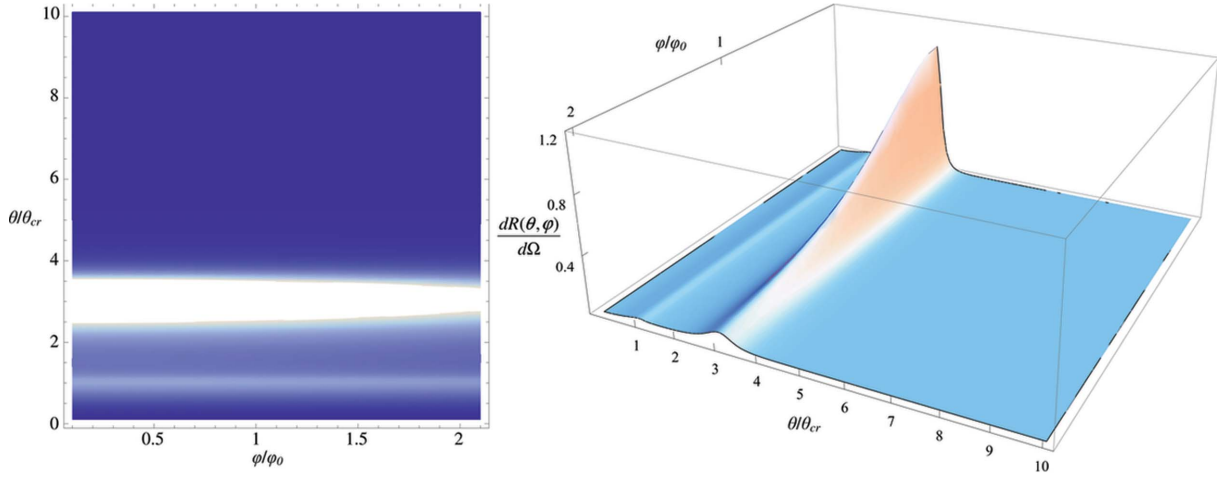

(*b*)

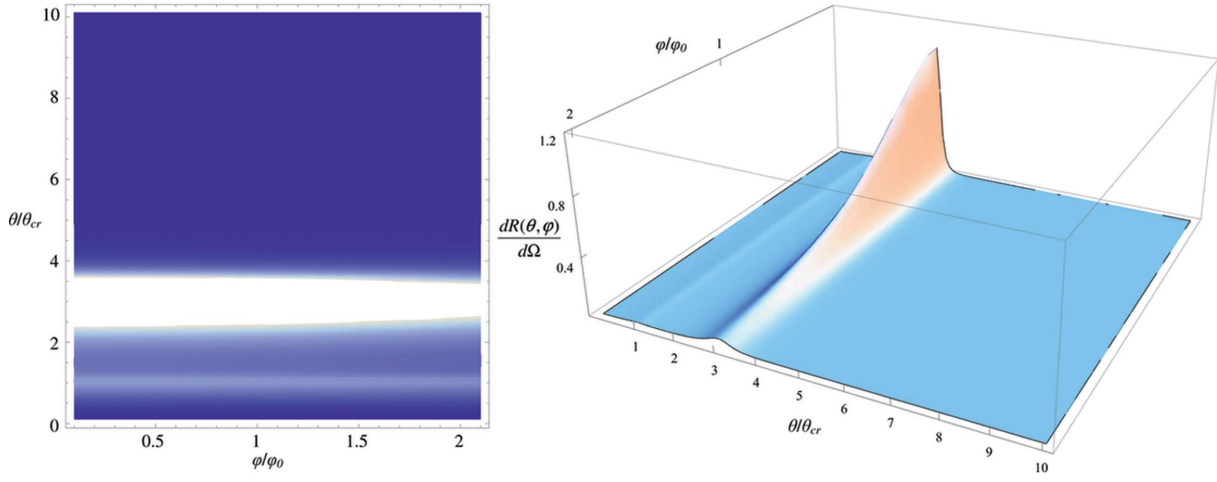

(*c*)

Figure 6
Normalized scans $[dR/d\Omega(\theta, \varphi)]/[dR/d\Omega(\theta_0, \varphi = 0)]$. Grazing-incidence angle θ_0/θ_{cr} is equal to 3. The r.m.s. roughness $k\sigma$ is equal to 80. Scattering polar and azimuth angles (θ, φ) are measured in units of (θ_{cr}, φ_0), $\theta_{cr} = (-\mathrm{Re}\chi)^{1/2} = 10^{-2.5}$ and $\varphi_0 = (k\ell)^{-1} = (5)^{-1}10^{-4}$; fractal index h is equal to 1/4 (*a*), 1/2 (*b*), 3/4 (*c*).

In a compartment with asymptotic behaviour of the $\mathrm{PSD_{1D}}(|q-q_0|)$ function for $\theta \gg \theta_0$ and $k\ell \gg 1$, the above yields a decreasing law for expression (21) of the DSI $\mathrm{d}R/\mathrm{d}\theta(\theta)$ scan

$$\frac{\mathrm{d}R}{\mathrm{d}\theta}(\theta)|_{\theta/\theta_0 \gg 1} \propto (\theta/\theta_0)^{-4-4h}. \quad (23)$$

The reader should note here that, with an increase in scattering angle θ, the statistical scattering factor [equation (32)] and the $\mathrm{PSD_{1D}}(q, q_0)$ function in the form (30) go on their asymptotical values with different 'θ-altering' speeds. For this reason, to extract the FSMI h in that way, it is preferable to use an actual straight-line slope of the statistical scattering factor $\eta_R(q, q_0)$ calculated in (32)–(35) in the measurement-window end of scattering angle θ, $\theta/\theta_0 \gg 1$.

4. Numerical run-through for probing deep into the present approach to the GISAXS problem

In this section, the results of numerical calculations for the specular and non-specular GISAXS by rough surfaces are presented staying in the scope of the present approach. Appropriate evaluations have been made using the averaged surface parameters such as the r.m.s. roughness $k\sigma$, correlation length $k\ell$ and FSMI h.

First, the specular $R_{\mathrm{spec}}(\theta_0)$ scans numerically simulated *versus* the grazing-incidence angle θ_0 are shown in Fig. 2, the angular window being $0 < \theta_0/\theta_{\mathrm{cr}} < 10$. The dimensionless r.m.s. roughness parameter $k\sigma$ is equal to (Fig. 2*a*) 40 and (Fig. 2*b*) 80.

Note that curves 1 in Fig. 2 correspond to the conventional Fresnel formula for the specular reflectivity $R_{\mathrm{spec}}(\theta_0)$ related to the specular GISAXS by a flat surface.

It is easy to see that in the case of $k\sigma = 40$ the $R_{\mathrm{spec}}(\theta_0)$ scans calculated by use of the Debye–Waller factor $f_{\mathrm{DW}}(q_0)$ and expression (20) along with equation (31) for the specular scattering factor $f(q_0)$ practically coincide with each other (curves 2 and 3 in Fig. 2*a*), whereas for $k\sigma = 80$ the curves 2 and 3 in Fig. 2(*b*) are about the same up to angles $\theta_0/\theta_{\mathrm{cr}} < 3$ and then sharply diverge for angles $\theta_0/\theta_{\mathrm{cr}} > 3$. In this case, the behaviour of curve 3 in Fig. 2(*b*) is determined by the specular scattering factor $f(q_0)$ as $0.25|k_z(q_0) - \kappa_z(q_0)|^4\sigma^4 \ll 1$.

Here we remind the reader again that in Fig. 2, curves 2 are calculated by use of the conventional Debye–Waller factor $f_{\mathrm{DW}}(q_0)$, whereas curves 3 are calculated using the specular scattering factor $f(q_0)$ in the form of equation (31) obtained in the frame of the present approach.

An assortment of computer simulations for the non-specular intensity distribution $\mathrm{d}R(\theta, \varphi)/\mathrm{d}\Omega$ and DSI $\mathrm{d}R/\mathrm{d}\theta(\theta)$ have been carried out according to expressions (19) and (21).

As it follows from an analysis of equations (19), (21), all of them support the previously made assertion that the 'Yoneda scattering' peak increases (decreases) with decreasing (increasing) the parameter $k\ell$ (and/or the grazing-incidence angle θ_0, $\theta_0 > \theta_{\mathrm{cr}}$).

Examples of the non-specular intensity distribution $\mathrm{d}R(\theta, \varphi)/\mathrm{d}\Omega$ and DSI $\mathrm{d}R/\mathrm{d}\theta(\theta)$, numerically simulated in the scope of the present approach, are depicted in Figs. 3–6 and Figs. 7–10. The calculations have been carried out for the diverse r.m.s. roughness σ and FSMI h; correlation length ℓ is assumed to be equal to 1.225 μm.

For clarity, the additional upper axis of $(q_0 - q)$ coordinate normalized to the value of $q_0 \times 10^{-5}$ is shown in Figs. 7–10, where $(q_0 - q)$ is the wavevector transfer at the scattering azimuth angle $\varphi = 0$ and $q = k\cos\theta$, $q_0 = k\cos\theta_0$, respectively.

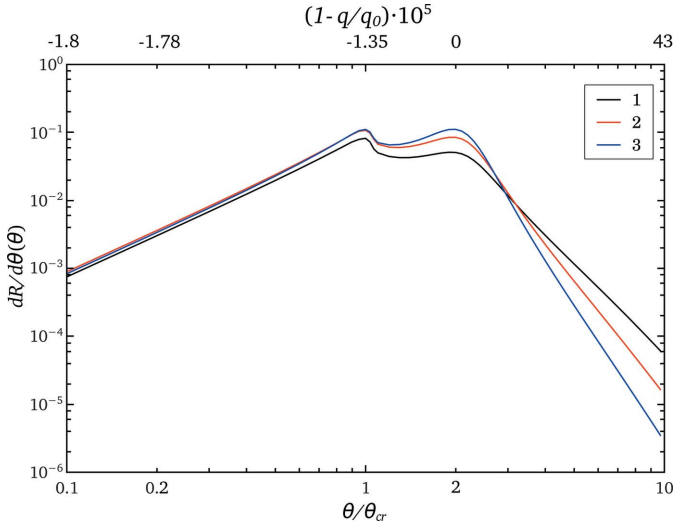

Figure 7
DSI scans of $\mathrm{d}R/\mathrm{d}\theta(\theta)$ numerically simulated using equation (21) along with equations (30) and (32)–(35). Grazing-incidence angle $\theta_0/\theta_{\mathrm{cr}}$ is equal to 2; the r.m.s. roughness $k\sigma$ is equal to 40; fractal index h is equal to: (curve 1) = 1/4; (curve 2) = 1/2; (curve 3) = 3/4.

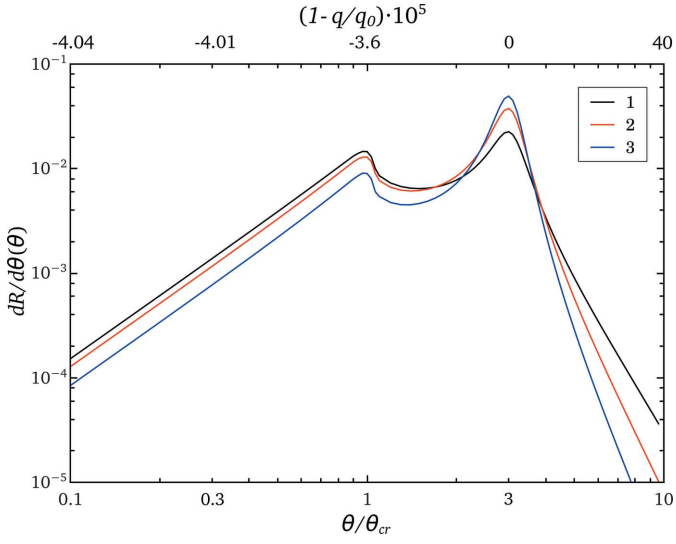

Figure 8
DSI scans of $\mathrm{d}R/\mathrm{d}\theta(\theta)$ numerically simulated using equation (21) along with equations (30) and (32)–(35). Grazing-incidence angle $\theta_0/\theta_{\mathrm{cr}}$ is equal to 3; the r.m.s. roughness $k\sigma$ is equal to 40; fractal index h is equal to: (curve 1) = 1/4; (curve 2) = 1/2; (curve 3) = 3/4.

Figs. 3–6 and Figs. 7–10 support the fact that the 'Yoneda scattering' peak decreases (increases) with decreasing (increasing) the grazing-incidence angle θ_0, $\theta_0 > \theta_{cr}$, even beyond the constraint $2k\sigma\theta_0 < 1$.

Herein, special attention must be paid to the fact that the FSMI h value is nothing else but the corresponding straight-line slopes of the DSI $dR/d\theta(\theta)$ in the log–log scale for $\theta/\theta_0 \gg 1$.

Indeed, using formula (21) along with equation (30), one can calculate the asymptotic value derivative of the expression $-\log[dR/d\theta(\theta)]$ and/or with respect to the variable $\log[\theta/\theta_0]$ or $\ln(q_0 - q)$.

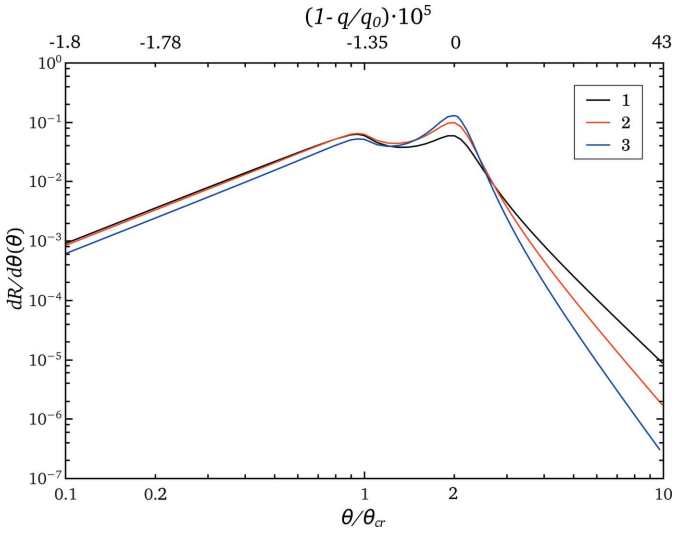

Figure 9
DSI scans of $dR/d\theta(\theta)$ numerically simulated using equation (21) along with equations (30) and (32)–35). Grazing-incidence angle θ_0/θ_{cr} is equal to 2; the r.m.s. roughness $k\sigma$ is equal to 80; fractal index h is equal to: (curve 1) = 1/4; (curve 2) = 1/2; (curve 3) = 3/4.

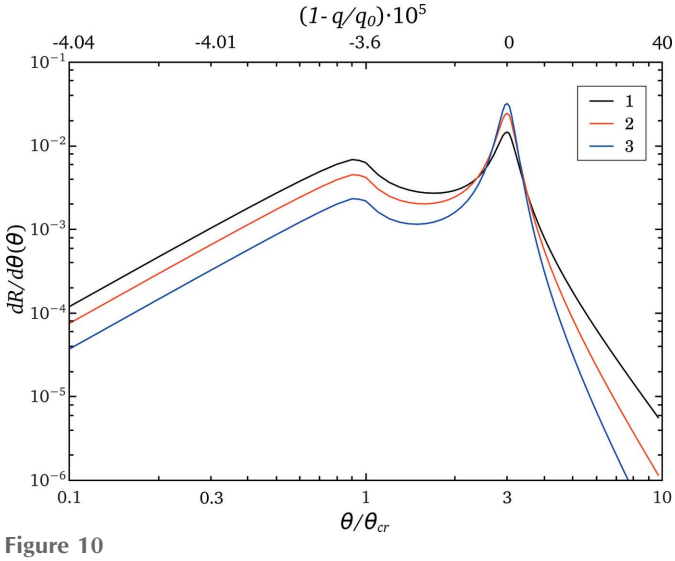

Figure 10
DSI scans of $dR/d\theta(\theta)$ numerically simulated using equation (21) along with equations (30) and (32)–35). Grazing-incidence angle θ_0/θ_{cr} is equal to 3; the r.m.s. roughness $k\sigma$ is equal to 80; fractal index h is equal to: (curve 1) = 1/4; (curve 2) = 1/2; (curve 3) = 3/4.

Table 1
The FSMI values h_{asym} computed at the angular point $\theta = 10\theta_{cr}$ according to expressions (24) and (25).

The incident angle θ_0/θ_{cr} is equal to (*a*) 2, (*b*) 3; correlation length $\ell = 0.1225$ μm.

	$k\sigma$	
	40	80
h	h_{asym}	h_{asym}
(*a*)		
1/4	[0.2812, 0.2497]	[0.2816, 0.2502]
1/2	[0.5415, 0.4996]	[0.5420, 0.2500]
3/4	[0.8019, 0.7499]	[0.8025, 0.7501]
(*b*)		
1/4	[0.3245, 0.2913]	[0.3250, 0.2919]
1/2	[0.5993, 0.5555]	[0.5999, 0.5557]
3/4	[0.8741, 0.8187]	[0.8748, 0.8695]

Accordingly, taken for $\theta/\theta_0 \gg 1$ they are equal to

$$\frac{d}{d\ln(\theta/\theta_0)}\left\{\log\left[-\frac{dR}{d\theta}(\theta,\theta_0)/\eta_R(\theta,\theta_0)\right]\right\}\Big|_{\theta/\theta_0\gg1} = 2 + 4h, \tag{24}$$

$$\frac{d}{d\ln(q_0 - q)}\left\{\log\left[-\frac{dR}{d\theta}(q,q_0)\left(\frac{q_0}{q}\right)^{1/2}/\eta_R(q,q_0)\right]\right\}\Big|_{\theta/\theta_0\gg1} = 1 + 2h, \tag{25}$$

where $(q_0 - q)$ is the wavevector transfer at the scattering azimuth angle $\varphi = 0$.

It should be noticed that estimate (25) is more accurate since it does not require one to expand the variable $\ln(q_0 - q)$ over the small values of θ, $\theta_0 \ll 1$.

Accordingly, the asymptotic FSMI values h_{asym} numerically calculated at the angle $\theta/\theta_{cr} = 10$ are listed in Table 1. It is seen that h_{asym} fit the true values of the FSMI h (assumed to evaluate the non-specular DSI scans) more accurately in the case of $\theta_0/\theta_{cr} = 2$ than for $\theta_0/\theta_{cr} = 3$.

5. Direct determination of the finish parameters of rough surfaces from the specular $R_{spec}(\theta_0)$ and non-specular $dR/d\theta(\theta)$ scans

Herein, implementation of the present approach is demonstrated on the example of the specular reflectivity $R_{spec}(\theta_0)$ and non-specular DSI $dR/d\theta(\theta)$ measured for the two solid samples: (*a*) α-quartz, reference surface plane $\{11\bar{2}0\}$ and (*b*) CdTe, reference surface plane {111}.

The surface of the α-quartz sample was finished by mechanical polishing with iron oxide powders that contained grains of different sizes. The sample was cleaned with ethanol just before the experimental measurements.

The surface of the CdTe sample was polished using the chemical mechanical polishing technique with potassium iodate reagents.

The experimental setup is drawn schematically in Fig. 11(*a*). It is designed on the basis of a goniometer of a triple-crystal X-ray spectrometer equipped with a triple-slit collimation

system. Both the Cu $K\alpha_1$ radiation tube and the one-dimensional scintillation detector are mobile in the θ plane, their angular displacements are controlled by angular encoders with precision up to 2 arcsec.

In order to decrease the intensity of parasitic scattering, the special vacuum tract waveguide is placed between the sample and scintillation detector slit, allowing one to decrease parasitic background scattering up to one order factor (Asadchikov *et al.*, 2003). The angular divergent FWHM $\delta\theta_0$ of the incident X-ray beam was approximately equal to 70 arcsec. The angular step $\Delta\theta_0$ was changed from 20 to 200 arcsec during the measurements. The detector slit width was constant and equal to 1000 µm in the case of the specular reflectivity measured, whereas it could be changed from 60 to 500 µm for collecting the DSI data.

The 'small-signal part' of the DSI scan was measured with the detector slit width increased to 500 µm, then normalized to the rest of the DSI scan that was measured with the detector slit width of 60 µm. The noise background level of the X-ray radiation was 0.3 counts s^{-1}. This means that for the specular reflectivity $R_{spec}(\theta_0)$ measured with sufficient accuracy the latter determines the angular interval $\{\theta_0\}$ in which it might be collected up to 10^{-6}–10^{-7} of the incident X-ray beam intensity.

In order to improve the signal-to-noise ratio and thus minimize the X-ray count measurement errors, the specular reflectivity and non-specular DSI scans are collected three times at each angular position, so their averaged values are assumed as the DSI scan data.

The specular $R_{spe}(\theta_0)$ and non-specular DSI $dR/d\theta(\theta)$ scans for both the α-quartz and CdTe samples measured and calculated are presented in Figs. 12 and 13.

Fig. 12 contains the experimentally measured and numerically simulated specular reflectivity $R_{spec}(\theta_0)$ scans of (*a*) α-quartz and (*b*) CdTe. From Fig. 12 it is clearly seen that for the r.m.s. roughness [(*a*) σ = 0.8 nm and (*b*) σ = 3.5 nm] the experimental $R_{spec}(\theta_0)$ scans match the theoretical ones rather well. In our case, measurements of the specular reflectivity in the angular ranges $\{\theta_{0i}\}$, $i = 1, 2, 3 \ldots$, up to $\theta_{0i}/\theta_{cr} = 5$ provide the maximum statistical error equal to 0.05 for α-quartz and 0.35 for CdTe.

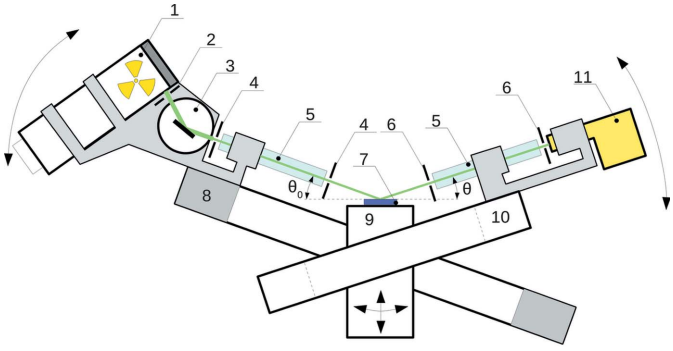

(*a*)

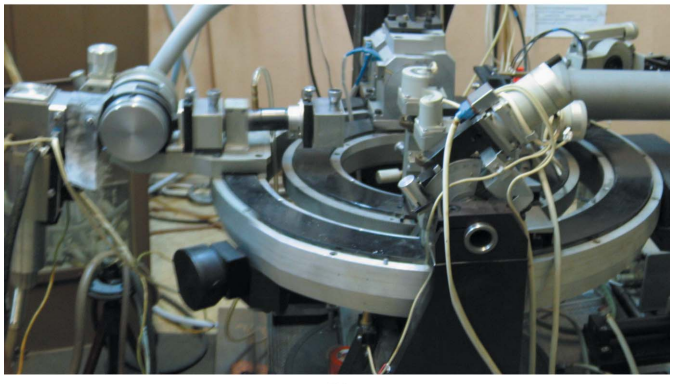

(*b*)

Figure 11
Schematic (*a*) and photo (*b*) of the GISAXS experimental setup. (*a*) 1, the X-ray radiation source tube; 2, 4, 6, aperture slits; 3, crystal monochromator; 5, vacuum X-ray path tube with both the end-side radiolucent windows; 7, sample; 8, ring-holder for the X-ray radiation source; 9, alignment table; 10, ring-holder for detector; 11, scintillation detector.

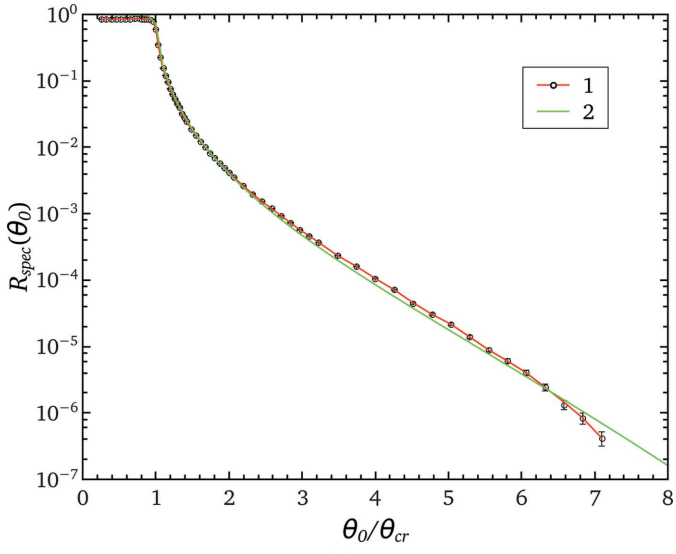

(*a*)

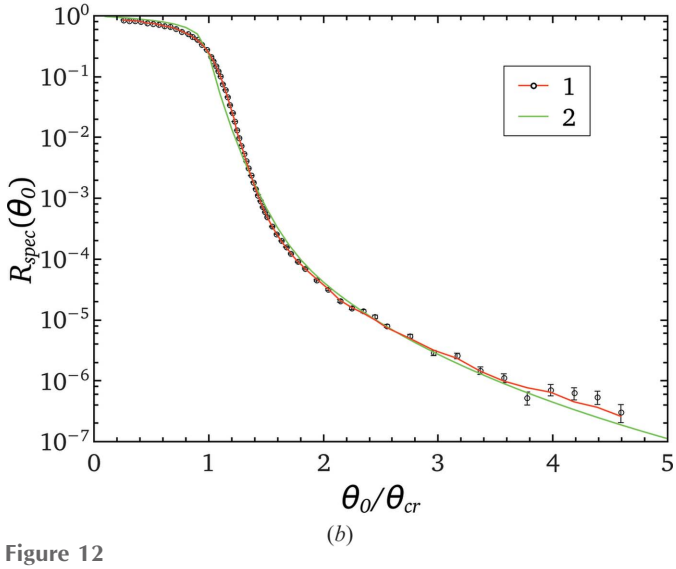

(*b*)

Figure 12
Specular $R_{spe}(\theta_0)$ scans experimentally measured (curves 1) and numerically simulated (curves 2) for the α-quartz sample in (*a*) and CdTe sample in (*b*). The r.m.s. roughness σ, correlation length ℓ and fractal index h chosen to match the measured and calculated scans to each other are equal to: (*a*) σ = 0.8 nm; (*b*) σ = 3.5 nm.

Both the experimental and theoretical DSI scans superposed at the 'Yoneda scattering peak' position, $\theta/\theta_{cr} \cong 1$, are shown in Fig. 13. The r.m.s. roughnesses σ are assumed to be the same as they are used for calculating the theoretical scans $R_{spec}(\theta_0)$ in Fig. 12.

As it follows from Fig. 13, the theoretical DSI scans are in good agreement with the theoretical ones for the corresponding values of the FSMI h = 1/4 and correlation length $\ell = 2.45$ µm in Fig. 13(a), FSMI h = 1/12 and correlation length $\ell = 0.1225$ µm in Fig. 13(b). In the angular ranges $\{\theta_i\}$, i = 1, 2, 3 . . . , up to $\theta_i/\theta_{cr} = 8$, the DSI measurements provide the maximum statistical error equal to 0.25 for α-quartz and 0.20 for CdTe.

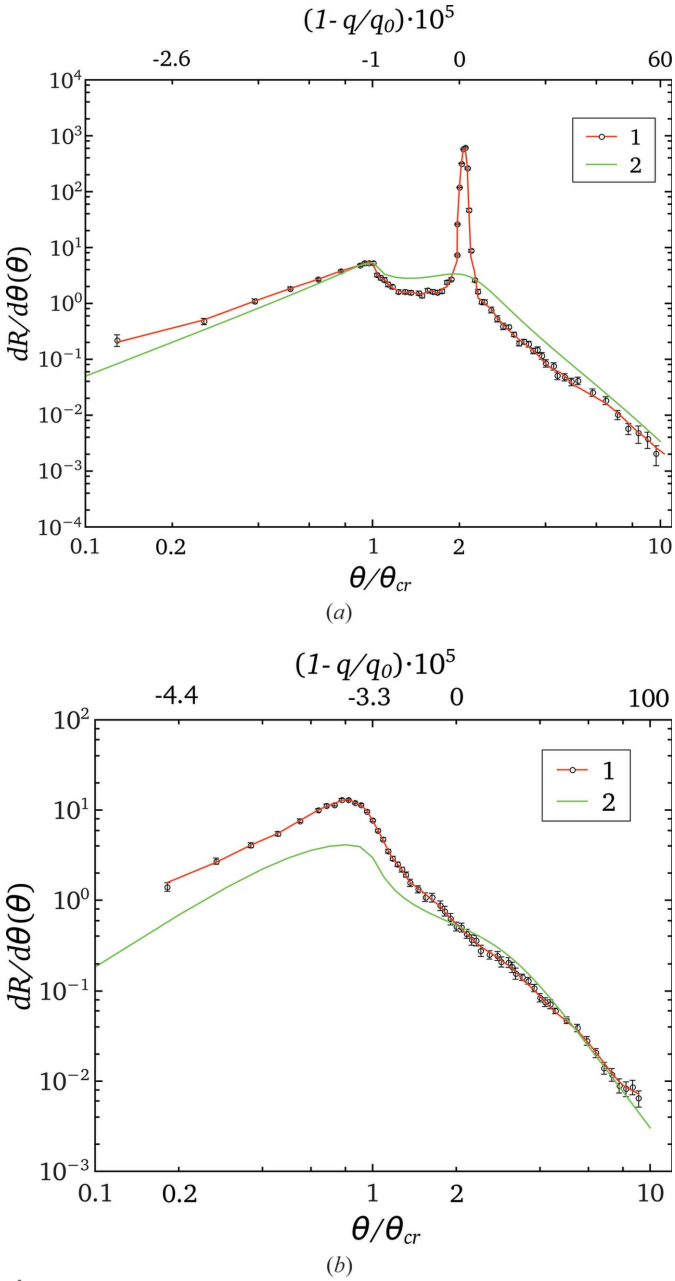

Figure 13
Non-specular DSI $dR/d\theta(\theta)$ scans experimentally measured (curves 1) and numerically simulated (curves 2) for the α-quartz sample in (a) and CdTe sample in (b). The r.m.s. roughness σ, correlation length ℓ and fractal index h chosen to match the measured and calculated scans to each other are equal to: (a) $\sigma = 0.8$ nm; (b) $\sigma = 3.5$ nm; (a) curve 2 $\ell = 2.45$ µm and h = 1/4; (b) curve 2 $\ell = 0.1225$ µm and h = 1/12.

It is interesting that the experimental DSI scans in Figs. 13(a) and 13(b) are rather different around the point $\theta = 2\theta_0$ where the specular scattering occurs. Indeed, a direct analysis shows that in the case of the CdTe sample (Fig. 13b) the specular scattering is less by an order of magnitude than the non-specular scattering, whereas in the case of the α-quartz sample (Fig. 13a) the experimental DSI peak at the point $\theta = 2\theta_0$ is mainly due to the specular scattering. From Fig. 13(a), the FWHM value about equal to 70 arcsec is nothing but the FWHM $\delta\theta_0$ of the incident X-ray beam.

6. Conclusion

In conclusion, based on the analytical and numerical results obtained, we can state that the present approach provides a plausible description of the GISAXS phenomenon beyond the constraint $2k\sigma\theta_0 < 1$. The plane **q**-eigenwave formalism allows one to derive integral equations (11a), (11b) that, in turn, can be used in a simple way to build up the first-order iteration solution [equations (14a), (14b)] for the reflected and transmitted plane **q**-eigenwaves propagating through the twofold rough medium.

Other key assumptions such as the Gaussian roughness statistics and K-correlation model of a rough surface that provides expressions (26) and (30) with $PSD_{2D}(|\mathbf{q} - \mathbf{q}_0|)$ and $PSD_{1D}(q, q_0)$ functions have been used to develop the present approach of the GISAXS theory.

From the run-through of the numerically simulated and experimentally measured specular $R_{spec}(\theta_0)$ and DSI $dR/d\theta(\theta)$ scans (see §§5, 6), the present approach allows one to directly estimate the surface finish parameters $\{\sigma, \ell, h\}$. With some confidence, it can be favourably applied to retrieve the surface finish parameters from experimental GISAXS data beyond the constraint $2k\sigma\theta_0 < 1$.

At this point, it should be noted once more that the present approach embraces the GISAXS problem even if other roughness statistics and non-fractal surface models have to be applied.

On the other hand, the question of whether the theoretical approach elaborated here on the whole is effective or whether it should be given up in favour of other approaches, which should be applied instead, remains a good topic for future work.

APPENDIX *A*

According to Kato (1980), the two-point isotropic cumulant correlation function $K_2(|\mathbf{x}_1 - \mathbf{x}_2|)$ is in general possessed of the properties: $K_2(x) = 1$ for $x = 0$ and $K_2(x) \to 0$ for $x/\ell \to \infty$ ($x = |\mathbf{x}|$, the lateral two-dimensional vector $\mathbf{x} = \mathbf{x}_1 - \mathbf{x}_2$ lies within the reference plane $z = 0$, ℓ is the correlation length).

To derive the expressions under consideration for the non-specular intensity distributions $dR/d\Omega(\theta,\varphi)$ and DSI $dR/d\theta(\theta)$, one needs to utilize the two-dimensional Fourier transform of the correlation function $K_2(x)$ that is referred to as the so-called power spectrum density function, in brief, the $PSD_{2D}(q)$ function, where the lateral two-dimensional vectors $\mathbf{q}, \mathbf{q}_0$ are parallel to the reference plane $z = 0$, $q = |\mathbf{q}|$, $q_0 = |\mathbf{q}_0|$ (see, *e.g.*, Church & Takacs, 1991; Asadchikov *et al.*, 2003).

Following Church & Takacs (1991), we use the *K*-correlation model for the $PSD_{2D}(|\mathbf{q}-\mathbf{q}_0|)$ function taken in the form

$$\mathrm{PSD}_{2D}(|\mathbf{q}-\mathbf{q}_0|) = \frac{4\pi h\ell^2}{\left[1+(|\mathbf{q}-\mathbf{q}_0|\ell)^2\right]^{1+h}}, \tag{26}$$

where h is the fractal surface model index (FSMI).

Here, the two-dimensional lateral vectors $\mathbf{q}$ and $\mathbf{q}_0$ are: $\mathbf{q} = k(\cos\theta\cos\varphi, \cos\theta\sin\varphi, 0)$ and $\mathbf{q}_0 = k\ (\cos\theta_0, 0, 0)$ (*cf.* Fig. 1).

Comprehensive arguments on the application of equation (26) to the $PSD_{2D}(|\mathbf{q}-\mathbf{q}_0|)$ function in the cases of solid surface interfaces have been discussed by Sinha *et al.* (1988), Church & Takacs (1991), Asadchikov *et al.* (2003).

In general (Church & Takacs, 1991), it is possible to write the $PSD_{2D}(q)$ function as a sum of several terms of the form of equation (26).

It should be noted that in accordance with expression (26) the cumulant correlation function $K_2(x)$ is equal to (*cf.* Church & Takacs, 1991)

$$K_2(x) = \frac{h(x/\ell)^h}{2^{h-1}\Gamma(h+1)} K_{-h}(x/\ell), \tag{27}$$

where $K_{-h}(x/\ell)$ is a modified Bessel function of the second kind.

Correspondingly, $K_2(0) = 1$ for $x = 0$ and in a limit of $x/\ell \to \infty$ it exponentially tends to zero as ($h \neq 1/2$)

$$K_2(x) = \frac{h(x/\ell)^h}{2^{h-1}\Gamma(h+1)}\left(\frac{\pi}{2x/\ell}\right)^{1/2}\exp(-x/\ell)[1+0(\ell/x)]. \tag{28}$$

It is interesting that for the FSMI $h = 1/2$ the cumulant correlation function [equation (27)] exactly coincides with the exponential expression $\exp(-x/\ell)$ for the height–height roughness correlation function (Sinha *et al.*, 1988).

In order to interpret the DSI $dR/d\theta(\theta;\theta_0)$-scan data, in addition to the $PSD_{2D}(|\mathbf{q}-\mathbf{q}_0|)$ function one needs to utilize the $PSD_{1D}(q, q_0)$ function that is defined as the integral of the $PSD_{2D}(|\mathbf{q}-\mathbf{q}_0|)$ function over the scattering azimuth angle φ:

$$\mathrm{PSD}_{1D}(q, q_0) = \int_{-\pi}^{\pi} d\varphi\, \mathrm{PSD}_{2D}(|\mathbf{q}-\mathbf{q}_0|). \tag{29}$$

After the straightforward routine calculations one obtains the following expression for the $PSD_{1D}(q, q_0)$ function ($k\ell \gg 1$ is assumed to be satisfied):

$$\mathrm{PSD}_{1D}(q, q_0) = \frac{4\pi h\ell}{(qq_0)^{1/2}\left[1+\ell^2(q-q_0)^2\right]^{1/2+h}}\frac{\Gamma\left(\frac{1}{2}\right)}{\Gamma(h+1)}\Gamma\left(h+\frac{1}{2}\right), \tag{30}$$

where $(q_0 - q)$ is the wavevector transfer at the scattering azimuth angle $\varphi = 0$ and $\Gamma(t)$ is the well known gamma function, $\Gamma(1/2) = (\pi)^{1/2}$.

APPENDIX *B*

By using solution (14*a*) for the non-averaged plane eigenwave amplitude $B_1(\mathbf{q})$ and taking into account the Gaussian statistics to evaluate $\overline{B_1(\mathbf{q})}$ and the Kato cumulant average of $\overline{[B_1(\mathbf{q})\cdot B_1^*(\mathbf{q})]}_{\mathrm{cum}}$, the calculations similar to analogous ones in Chukhovskii (2011) yield the following analytical expressions for the specular and non-specular scattering factors, $f(q_0)$ and $\eta_R(q, q_0)$, namely

$$f(q_0) = \left|1-\exp[-0.5(\kappa_z(q_0)-k_z(q_0))^2\sigma^2] + \exp[-0.5(\kappa_z(q_0)+k_z(q_0))^2\sigma^2]\right|^2 \tag{31}$$

and

$$\eta_R(q, q_0) = \eta_{R1}(q, q_0) - \eta_{R2}(q, q_0), \tag{32}$$

where

$$\begin{aligned}
&\eta_{R1}(q, q_0) = 0.25k^2\sigma^2\times\\
&\{|T_1(q)|^2(|\alpha|^{-2}(1+\exp[\mathrm{Im}^2(\alpha+\beta)]\mathrm{Erfc}[\mathrm{Im}(\alpha+\beta)]\\
&\quad -2\mathrm{Re}[\exp(-\alpha^2)\mathrm{Erfc}[-i\alpha]])\\
&\quad +|\beta|^{-2}|R_1(q_0)|^2(1+\exp[\mathrm{Im}^2(\alpha+\beta)]\mathrm{Erfc}[\mathrm{Im}(\alpha+\beta)]\\
&\quad -2\mathrm{Re}[\exp(-\beta^2)\mathrm{Erfc}[-i\beta]]) + 2\mathrm{Re}[\beta^{-1}(\alpha^*)^{-1}R_1(q_0)\\
&\quad \times(1+\exp[-(\beta-\alpha^*)^2]\mathrm{Erfc}[-i(\beta-\alpha^*)]\\
&\quad -\exp[-(\alpha^*)^2]\mathrm{Erfc}[i\alpha^*] - \exp[-\beta^2]\mathrm{Erfc}[-i\beta])])\\
&\quad +|T_1(q_0)|^2(|\mu|^{-2}(1+\exp[\mathrm{Im}^2(\mu+\nu)]\mathrm{Erfc}[-\mathrm{Im}(\mu+\nu)]\\
&\quad -2\mathrm{Re}[\exp(-\mu^2)\mathrm{Erfc}[i\mu]])\\
&\quad +\nu^{-2}|R_1(q)|^2(1+1+\exp[\mathrm{Im}^2(\mu+\nu)]\mathrm{Erfc}[-\mathrm{Im}(\mu+\nu)]\\
&\quad -2\mathrm{Re}[\exp(-\nu^2)\mathrm{Erfc}[i\nu]])\\
&\quad +2\mathrm{Re}[\nu^{-1}(\mu^*)^{-1}R_1(q)(1+\exp[-(\nu-\mu^*)^2]\mathrm{Erfc}[i(\nu-\mu^*)]\\
&\quad -\exp[-(\mu^*)^2]\mathrm{Erfc}[-i\mu^*] - \exp[-\nu^2]\mathrm{Erfc}[i\nu])])\}
\end{aligned} \tag{33}$$

$$\begin{aligned}
\eta_{R2}(q, q_0) = 0.25k^2\sigma^2\Big|&T_1(q)(\alpha^{-1}\exp[-\alpha^2]\mathrm{Erfc}[-i\alpha]\\
&+\beta^{-1}R_1(q_0)\exp[-\beta^2]\mathrm{Erfc}[-i\beta]-1)\\
&+T_1(q_0)(\mu^{-1}\exp[-\mu^2]\mathrm{Erfc}[i\mu]\\
&+\nu^{-1}R_1(q)\exp[-\nu^2]\mathrm{Erfc}[i\nu]-1)\Big|^2.
\end{aligned} \tag{34}$$

In the above, there is the complementary error function $\mathrm{Erfc}[w]$ for complex argument w that is a quantity of some combinations of the dimensionless z-component wavevectors related to the diverse X-ray scattering processes of the plane $\mathbf{q}$-waves (*cf.* Chukhovskii, 2011):

$$\alpha = 2^{-1/2}\sigma\big[\kappa_z(q) + k_z(q_0)\big],\ \beta = 2^{-1/2}\sigma\big[\kappa_z(q) - k_z(q_0)\big],$$
$$\mu = 2^{-1/2}\sigma\big[\kappa_z(q_0) + k_z(q)\big],\ \nu = 2^{-1/2}\sigma\big[\kappa_z(q_0) - k_z(q)\big]. \quad (35)$$

Acknowledgements

Valuable discussions with V. E. Asadchikov, I. V. Kozhevnikov and A. M. Polyakov are gratefully acknowledged. The authors also thank Yu. O. Volkov for valuable comments on the manuscript.

References

Andronov, A. A. & Leontovich, M. A. (1926). *Z. Phys. B*, **38**, 485–495.
Asadchikov, V. E., Kozhenikov, I. V. & Krivonosov, Yu. S. (2003). *Sov. Phys. Crystallogr. Rep.* **48**, 836–850.
Boer, D. K. G. de (1994). *Phys. Rev. B*, **49**, 5817–5820.
Boer, D. K. G. de (1995). *Phys Rev. B*, **51**, 5297–5305.
Boer, D. K. G. de (1996). *Phys Rev. B*, **53**, 6048–6064.
Chukhovskii, F. N. (2009). *Acta Cryst.* A**65**, 39–45.
Chukhovskii, F. (2011). *Acta Cryst.* A**67**, 200–209.
Chukhovskii, F. N. (2012). *Acta Cryst.* A**68**, 505–512.
Church, E. L. & Takacs, P. Z. (1991). *Proc. SPIE*, **1530**, 71–85.
Kato, N. (1980). *Acta Cryst.* A**36**, 763–769.
Kozhevnikov, I. V. (2010). *Crystallogr. Rep.* **55**, 539–545.
Kozhevnikov, I. V. & Pyatakhin, M. V. (2000). *J. X-ray Sci. Technol.* **8**, 253–275.
Névot, L. & Croce, P. (1980). *Rev. Phys. Appl.* **15**, 761–779.
Petrashen', P. V., Kov'ev, E. K., Chukhovskii, F. N. & Degtyarev, Yu. L. (1983). *Solid State Phys.* **25**, 1211–1214.
Pietsch, U., Holy, V. & Baumbach, T. (2004). *High-Resolution X-ray Scattering – From Thin Films to Lateral Nanostructures.* Berlin: Springer Verlag.
Renaud, G., Lazzari, R. & Leroy, F. (2009). *Surf. Sci. Rep.* **64**, 255–380.
Salikhov, S. V., Chukhovskii, F. N. & Polyakov, A. M. (2011). *J. Surf. Invest.* **5**, 887–897.
Schmidbauer, M., Schäfer, P., Besedin, S., Grigoriev, D., Köhler, R. & Hanke, M. (2008). *J. Synchrotron Rad.* **15**, 549–557.
Sinha, S. K., Sirota, E. B., Garoff, S. & Stanley, H. B. (1988). *Phys. Rev. B*, **38**, 2297–2311.
Vinogradov, A. V., Zorev, N. N., Kozhevnikov, I. V. & Yakushkin, I. G. (1985). *Sov. Phys. JETF*, **62**, 1225–1233.
Wong, W. K., Wang, D., Benoit, R. T. & Barthol, P. (1991). *Proc. SPIE*, **1530**, 86–103.
Yoneda, Y. (1963). *Phys. Rev.* **131**, 2010–2013.